Targeting SLC7A11 improves efferocytosis by dendritic cells and wound healing in diabetes

https://doi.org/10.1038/s41586-022-04754-6

Received: 18 August 2021

Accepted: 11 April 2022

Sophia Maschalidi[1,2]✉, **Parul Mehrotra**[1,2,9], **Burcu N. Keçeli**[1,2,9], **Hannah K. L. De Cleene**[1,2], **Kim Lecomte**[2,3], **Renée Van der Cruyssen**[2,4], **Pauline Janssen**[5], **Jonathan Pinney**[6,7], **Geert van Loo**[2,3], **Dirk Elewaut**[2,4], **Ann Massie**[5], **Esther Hoste**[2,3] & **Kodi S. Ravichandran**[1,2,6,7,8]✉

Chronic non-healing wounds are a major complication of diabetes, which affects 1 in 10 people worldwide. Dying cells in the wound perpetuate the inflammation and contribute to dysregulated tissue repair[1–3]. Here we reveal that the membrane transporter SLC7A11 acts as a molecular brake on efferocytosis, the process by which dying cells are removed, and that inhibiting SLC7A11 function can accelerate wound healing. Transcriptomics of efferocytic dendritic cells in mouse identified upregulation of several SLC7 gene family members. In further analyses, pharmacological inhibition of SLC7A11, or deletion or knockdown of *Slc7a11* using small interfering RNA enhanced efferocytosis in dendritic cells. *Slc7a11* was highly expressed in dendritic cells in skin, and single-cell RNA sequencing of inflamed skin showed that *Slc7a11* was upregulated in innate immune cells. In a mouse model of excisional skin wounding, inhibition or loss of SLC7A11 expression accelerated healing dynamics and reduced the apoptotic cell load in the wound. Mechanistic studies revealed a link between SLC7A11, glucose homeostasis and diabetes. SLC7A11-deficient dendritic cells were dependent on aerobic glycolysis using glucose derived from glycogen stores for increased efferocytosis; also, transcriptomics of efferocytic SLC7A11-deficient dendritic cells identified increased expression of genes linked to gluconeogenesis and diabetes. Further, *Slc7a11* expression was higher in the wounds of diabetes-prone *db/db* mice, and targeting SLC7A11 accelerated their wound healing. The faster healing was also linked to the release of the TGFβ family member GDF15 from efferocytic dendritic cells. In sum, SLC7A11 is a negative regulator of efferocytosis, and removing this brake improves wound healing, with important implications for wound management in diabetes.

Billions of cells in the body are turned over on a daily basis via apoptosis. These cells are then recognized and removed by phagocytes via the process of efferocytosis[1]. Defects in efferocytosis are associated with non-resolving inflammation leading to chronic inflammatory conditions[2,3]. Dendritic cells (DCs) are a heterogenous group of phagocytes that are present in nearly all tissues. DCs display multiple phagocytic and pathogen-recognition receptors and help maintain tissue homeostasis through regulation of innate and adaptive immunity[4]. Although apoptotic cell uptake by DCs has long been recognized, it has been studied primarily in the context of antigen presentation and adaptive immunity[5–8]. In comparison with macrophages, much less is known about the molecular regulation of DC efferocytosis and its relevance to limiting inflammation.

As the largest organ in the body, our skin acts as a barrier to protect internal tissues from extreme temperature, water loss, ultraviolet radiation, microbial and chemical insults, and injury. Tissue repair after skin injury involves the clearance of apoptotic cells by phagocytes at the wound site as part of the process of resolving the inflammation and restoring the barrier[9,10]. Chronic non-healing wounds, such as those associated with diabetes, ageing or vascular disease, severely affect quality of life and increase the risk of infection[11]. Homeostasis in the healthy skin is maintained by immune cells, including DCs, macrophages and T cells, that populate the tissue. Langerhans cells residing in the epidermis and DCs in the dermis maintain surveillance by capturing dead cells or pathogens and presenting them to effector T cells[12,13]. Resident or recruited macrophages[14,15] and neutrophils[16] have been linked to wound healing dynamics; however, the contribution of DCs to injury repair is less well defined. Here, while characterizing gene programmes in DCs engulfing apoptotic cells, we unexpectedly discover that the plasma membrane protein SLC7A11 acts as a brake on DC-mediated efferocytosis and reveal its relevance to cutaneous wound healing.

---

[1]Unit for Cell Clearance in Health and Disease, VIB Center for Inflammation Research, Ghent, Belgium. [2]Department of Biomedical Molecular Biology, Ghent University, Ghent, Belgium. [3]Unit for Cellular and Molecular Pathophysiology, VIB Center for Inflammation Research, Ghent, Belgium. [4]Laboratory for Molecular Immunology and Inflammation, Department of Rheumatology, Ghent University Hospital, Ghent, Belgium. [5]Laboratory of Neuro-Aging and Viro-Immunotherapy, Center for Neurosciences (C4N), Vrije Universiteit Brussel, Brussels, Belgium. [6]The Center for Cell Clearance, University of Virginia, Charlottesville, VA, USA. [7]Department of Microbiology, Immunology, and Cancer Biology, and the Center for Cell Clearance, University of Virginia, Charlottesville, VA, USA. [8]Division of Immunobiology, Department of Pathology and Immunology, Washington University School of Medicine, St Louis, MO, USA. [9]These authors contributed equally: Parul Mehrotra, Burcu N. Keçeli. ✉e-mail: sophia.maschalidi@irc.vib-ugent.be; kodi@wustl.edu

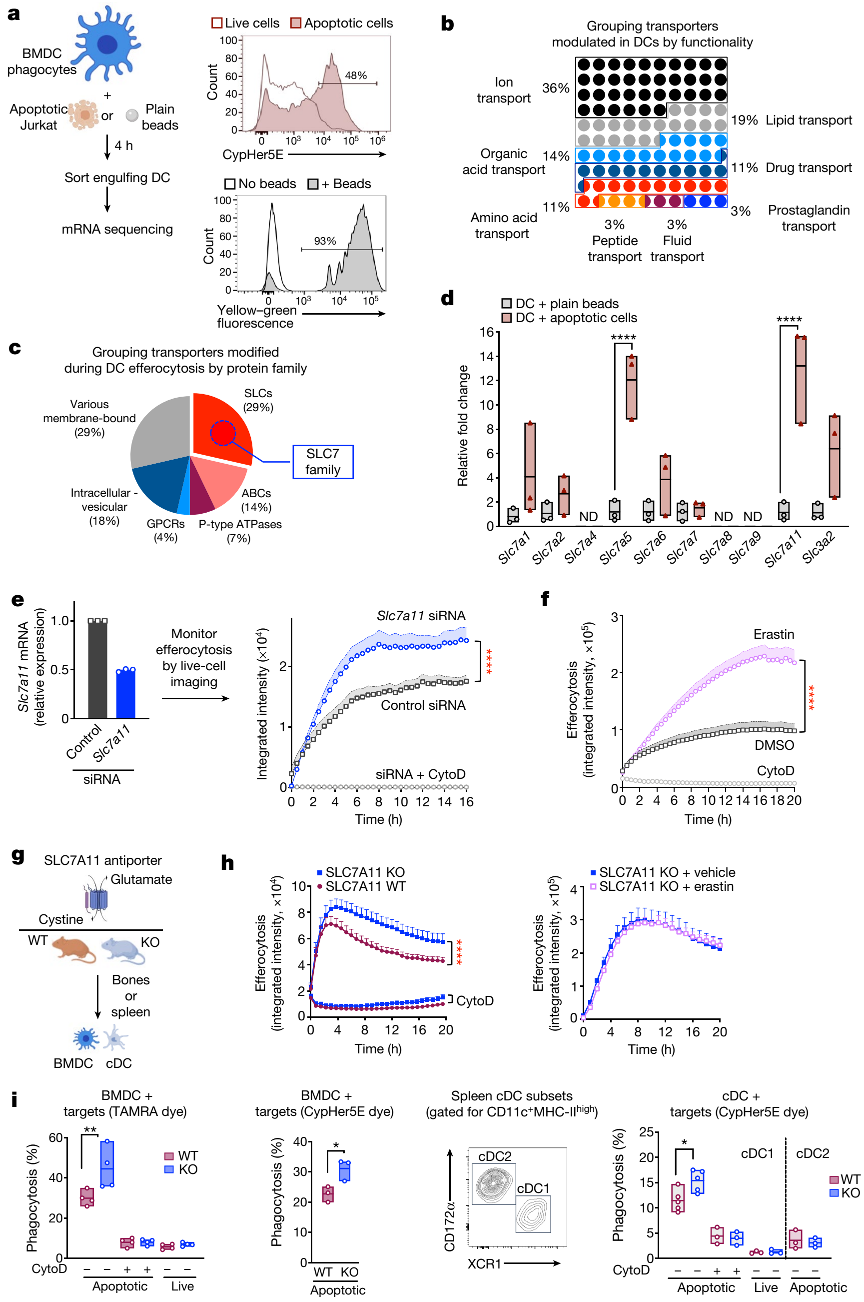

Fig. 1 | SLC7A11 acts as a brake on DC engulfment of apoptotic cells. **a**, Schematic of phagocytosis assays using BMDCs fed apoptotic human Jurkat cells, live cells or 2-µm fluorescent beads. Histograms illustrate fluorescence derived from the targets in efferocytic DCs. **b**, **c**, Genes associated with transporter activity uniquely modulated after efferocytosis, categorized by function (**b**) and protein family (**c**). Data are from four independent replicates. ABCs, ATP-binding cassette transporters; GPCRs, G-protein-coupled receptors. **d**, Expression of SLC7 family genes after phagocytosis as in **a**, determined by quantitative PCR with reverse transcription (RT–qPCR). Data represent 3 biological replicates per condition. Two-way ANOVA with Sidak's multiple comparison test. ND, not detected. **e**, **f**, *Slc7a11* siRNA (**e**) or erastin (**f**) increase efferocytosis of apoptotic cells (labelled with pHrodo Green), measured by Incucyte live-cell imaging (pHrodo Green calibrated units/µm^2/image). **e**, $n = 3$ (control siRNA and Slc7a11 siRNA), $n = 4$ (siRNA + CytoD). **f**, $n = 6$ (DMSO), $n = 4$ (erastin), $n = 4$ (CytoD). **g**, Schematic of SLC7A11 transport activity and the mice used. **h**, Kinetics of efferocytosis by SLC7A11 wild-type (WT) and SLC7A11-KO BMDCs treated with erastin or vehicle. Left, $n = 8$ (SLC7A11 WT, SLC7A11-KO, SLC7A11 WT + CytoD), $n = 6$ (SLC7A11 KO + CytoD). Right, $n = 3$ per condition. **i**, Efferocytosis of TAMRA- or CypHer5E-labelled apoptotic Jurkat cells compared between control and SLC7A11-KO BMDCs (left and second from left). Purified cDC1 and cDC2 subsets (centre) were tested for phagocytosis with apoptotic and live Jurkat cells at a 1:5 phagocyte:target ratio for 4 h (right). Data from $n = 3$–5 biological replicates. One-way ANOVA with Dunnett's multiple comparisons test. Floating bars (**d**, **i**) show the range of values, dots show independent replicates and the line denotes the mean. All live-cell imaging data (**e**, **f**, **h**) are expressed as mean ± s.e.m.; one-way ANOVA with Tukey's multiple comparisons test. In all figures, $^*P < 0.05$, $^{**}P < 0.01$, $^{***}P < 0.001$, $^{****}P < 0.0001$, NS, not significant.

Regulation of SLCs in efferocytic DCs

To define gene signatures initiated in DCs during efferocytosis, we incubated primary mouse bone-marrow DCs (BMDCs) as phagocytes with labelled apoptotic human Jurkat cells, purified the engulfing DCs, and performed RNA-sequencing (RNA-seq) analysis (Fig. 1a). We used this cross-species approach to distinguish the RNA from mouse DCs from the apoptotic cargo-derived human RNA. We also used fluorescent microspheres (beads) as targets to control for phagocytosis. In our analysis, we focused on differentially expressed genes associated with transporter activity, based on the initial hypothesis that DCs may have molecular features that differ from other phagocytes. We found significant alterations in genes encoding membrane transporters with diverse functionalities, including those that passage ions, lipids and amino acids (Fig. 1b). Of note, the solute carrier (SLC) family of genes represented 29% of the differentially expressed transporters in efferocytic DCs (Fig. 1c). SLCs represent the second largest gene family in the human genome (after the G-protein-coupled receptors) and mediate transport of metabolites and solutes across cellular membranes. SLCs are also linked to more than 100 human diseases and are implicated in efferocytosis by other phagocytes[17] (Fig. 1c). In efferocytic DCs, SLC genes coding for amino acid metabolism and carbohydrate catabolism were upregulated, whereas SLC genes linked to oxidative phosphorylation and fatty acid transport were downregulated (Extended Data Fig. 1a).

Amino acid transport is fundamental for nutrient supply and supports key functions of immune cells[18,19], including DCs[20]. Thus, we examined cationic (SLC7A1, 2, 3 and 4) and dimeric or heteromeric amino acid transporters (SLC7A5, 6, 7, 8, 9, 10 and 11), as well as SLC3A2, which helps to chaperone or facilitate localization of some SLC7 members[21]. The largest increases within the SLC7 family gene expression in efferocytic DCs were in *Slc7a5* and *Slc7a11* (Fig. 1d).

SLC7A11 is a brake for DC efferocytosis

To test the relevance of these SLC7 family amino acid transporters, we performed small interfering RNA (siRNA)-mediated knockdown in BMDCs followed by efferocytosis using both a flow cytometry-based assay and live-cell imaging. Interfering with *Slc7a11* expression consistently led to greater efferocytosis by DCs (Fig. 1e). SLC7A11 is the subunit of the cysteine-glutamate antiporter system x_c^- that regulates exchange of intracellular glutamate for extracellular cysteine, a rate-limiting precursor for synthesis of the antioxidant glutathione (GSH). SLC7A11 is also linked to neurological diseases[22–26], viral infections[27–29] and cancers[30,31], and drugs targeting SLC7A11 are being tested in clinical trials. In our assays, knockdown or pharmacological inhibition of *Slc7a5* showed a trend towards increased efferocytosis, although this was not statistically significant, whereas *Slc7a1* inhibition did not affect BMDC efferocytosis (Extended Data Fig. 1b–e).

Given that expression of SLC7A11 increases robustly during efferocytosis, its function as a negative regulator of efferocytosis was unexpected. We therefore used additional pharmacological and genetic approaches. Inhibition of SLC7A11 with the drug erastin caused an increase in efferocytosis (Fig. 1f), whereas it did not affect the phagocytosis of *Escherichia coli* bioparticles by DCs (Extended Data Fig. 2a). Although erastin is an inducer of ferroptosis in cancer cells[32–34]), another ferroptosis-inducing compound, ML-162 (ref. [32], did not enhance efferocytosis (Extended Data Fig. 2b). Moreover, the antioxidant ferrostatin-1 (ref. [35]), a potent inhibitor of ferroptosis, did not reverse the enhanced DC efferocytosis due to SLC7A11 inhibition (Extended Data Fig. 2c). Although erastin treatment did reduce intracellular levels of GSH (Extended Data Fig. 2d), it only modestly increased lipid accumulation of reactive oxygen species (ROS) (Extended Data Fig. 2f) and did not affect DC viability (Extended Data Fig. 2e). When we assessed the contribution of GSH and ROS, neither supplementation nor depletion of GSH affected the enhanced efferocytosis of DCs with knockout or inhibition of SLC7A11 (Extended Data Fig. 3a, b). Ameliorating ROS with the compound carbonyl cyanide *p*-(trifluoromethoxy) phenylhydrazone (FCCP) or scavenging ROS with MitoTEMPO partially reversed the enhanced efferocytosis after SLC7A11 inhibition, although this effect was not statistically significant under the conditions tested. Thus, although the effect of SLC7A11 inhibition may be partly due to ROS, this is not sufficient to explain the enhanced efferocytosis (Extended Data Fig. 3c, d). The effect of erastin was also mimicked by excess glutamate to 'block' the cysteine uptake via SLC7A11, although the glutamate effect was partial (Extended Data Fig. 2g) perhaps owing to the lower SLC7A11 inhibition by glutamate compared to erastin[36]. By contrast, addition of *N*-acetylcysteine (NAC), a synthetic precursor of cysteine, reversed the enhanced efferocytosis of erastin-treated DC (Extended Data Fig. 2h), suggesting that cysteine transport via SLC7A11 is an important component of the increased efferocytosis.

As a genetic approach, we compared purified primary splenic conventional DCs from control and SLC7A11-deficient mice. We noted enhanced uptake by SLC7A11-deficient type I conventional DCs (cDC1s) but not cDC2s. Similarly, ex vivo-generated BMDCs lacking SLC7A11 displayed greater efferocytosis (Fig. 1g–i). This effect was seen with apoptotic targets labelled with pH-insensitive (TAMRA) or pH-sensitive (CypHer5E) dyes (Fig. 1i), and was abrogated by blocking cytoskeletal rearrangement with cytochalasin D (CytoD) (Fig. 1h, i). The increased uptake scored in these assays was not the result of defective digestion of apoptotic corpses, as control and SLC7A11-deficient DCs showed similar degradation of CellTrace Violet-labelled apoptotic cells (Extended Data Fig. 1f). Further, there was no additive increase in efferocytosis of SLC7A11-deficient DCs treated with erastin, supporting the specificity of the erastin (Fig. 1h). Notably, neither peritoneal macrophages from wild-type mice treated with erastin nor BMDMs from SLC7A11-deficient mice displayed enhanced efferocytosis in these conditions (Extended Data Fig. 1g, h). Finally, the SLC7A11-deficient DCs did not show an enhanced uptake of live cells (Fig. 1i). Thus, these data collectively suggest that SLC7A11 acts as brake on DC efferocytosis.

SLC7A11 blockade accelerates skin wound healing

As the continued presence of uncleared apoptotic cells is linked to chronic inflammation, we assessed gene expression profiles of SLCs in resident DC subsets in the spleen, lung or skin. Mining publicly available datasets (ImmGen) and comparing them via Triwise plots revealed that *Slc7a11* is most highly expressed in skin-resident DCs (Fig. 2a). By contrast, *Slc7a5* is expressed at higher levels in the spleen and lung DCs. Previous reports have suggested that depletion of epidermal Langerin$^+$ cells enhances cutaneous wound healing[37], whereas depletion of dermal CD11c$^+$ DCs delays wound closure[38]. Thus, we explored the link between SLC7A11 and DCs during skin wound healing.

When we tested purified dermal DCs isolated from the ears of SLC7A11-deficient mice, cDC1 cells showed enhanced efferocytosis; in comparison, Langerhans cells and cDC2 were poor engulfers ex vivo, and their phagocytic capacity was unaltered by SLC7A11 deficiency (Fig. 2b, Extended Data Fig. 4a). Although CD64$^+$ macrophages were able to engulf apoptotic cells, SLC7A11 deficiency did not modify their uptake (Fig. 2b). Histology of wounded skin tissue showed SLC7A11 colocalizing with the DC marker CD11c (Fig. 2c) but not fibroblasts (Extended Data Fig. 4b). Additionally, CD11c$^+$ DCs were proximal to and appeared to capture cleaved caspase-3$^+$ apoptotic corpses (Fig. 2d).

When we mined a human disease genetic association database[39], *SLC7A11* was most closely associated with skin diseases such as eczematoid dermatitis and recurrent skin infections (Extended Data Table 1). Further, probing single-cell transcriptomics data from inflammatory skin lesions in mouse that develop into verrucous carcinomas (Methods), we uncovered increased expression of *Slc7a11* in the innate immune cells (Fig. 2e), including several DC subsets (Extended Data Fig. 4c, d). *Slc7a11* expression also increased in total skin lysates after full-thickness wounding, along with genes linked to wounding such as *Tgfb1* and *Tnf* (Fig. 2f).

Next, we tested whether interfering with SLC7A11 function affected wound healing dynamics. We topically administered imidazole ketone erastin[40] (IKE), a metabolically stable and water-soluble version of erastin, to mice after full-thickness skin wounding (on day 0 to day 2). However, administering erastin alone did not improve wound healing

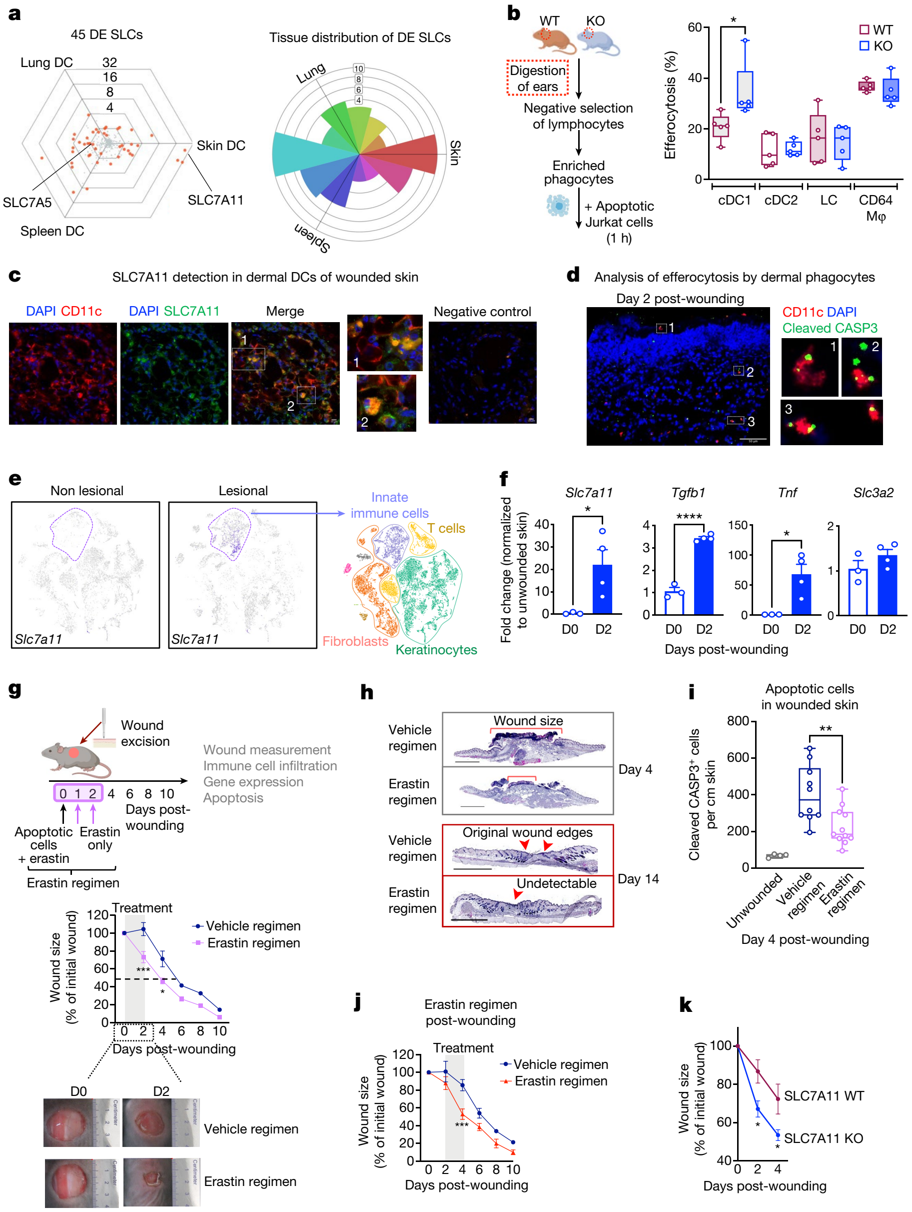

Fig. 2 | Accelerated skin wound healing in the context of SLC7A11 blockade. **a**, Left, hexagonal Triwise diagram visualizing relative expression levels of differentially expressed (DE) (orange) or non-differentially expressed (grey) SLC family genes among DCs from lung, spleen and skin. Proximity represents upregulation in more than one population, and the distance from the origin represents the strength of expression. Right, rose plot depicts the 45 differentially expressed genes grouped in bins and by DC subtype in which the genes are most highly expressed. **b**, Efferocytosis by dermal phagocytes enriched from the ears of SLC7A11-deficient and control littermates (*n* = 5 per group; unpaired two-tailed *t*-test). **c**, **d**, Left, localization of CD11c$^+$ phagocytes and SLC7A11 in skin on day 2 after wounding (**c**) and capturing apoptotic (cleaved caspase-3 (CASP3)-positive) corpses (**d**). Outlined regions are expanded on the right. Nuclei are labelled with DAPI. Secondary antibodies were used as negative control. Scale bars: 10 µm (**c**), 50 µm (**d**). **e**, Left, uniform manifold approximation and projection (UMAP) clustering of cells isolated from non-lesional and lesional skin (Methods), highlighting expression of *Slc7a11*. Right, *t*-distributed stochastic neighbour embedding (*t*-SNE) plot of cells in lesional skin after single-cell RNA-sequencing (scRNA-seq) analysis. **f**, Gene expression in skin lysates of day (D)0 (unwounded; *n* = 3) and day 2 (wounded; *n* = 4) mice. Unpaired two-tailed *t*-test. **g**, **j**, Wound healing dynamics of wild-type mice treated with erastin or vehicle regimen on day 0 to day 2 (**g**; *n* = 8 per group) or day 2 to day 4 (**j**; *n* = 10 (vehicle), *n* = 9 (erastin)). Data representative of 4 independent experiments. **h**, **i**, Haematoxylin and eosin-stained wounded skin sections (**h**) and quantification of apoptotic cells (**i**) in unwounded (*n* = 4) and wounded skin (*n* = 10 (DMSO); *n* = 11 (erastin regimen)) at day 4 after wounding. Unpaired *t*-test. Scale bars, 100 µm. **k**, Wound healing dynamics comparing SLC7A11 wild-type and SLC7A11-KO mice (*n* = 6 per group). **g**, **j**, **k**, Two-way ANOVA with multiple comparisons. In box plots (**b**, **i**), the centre line denotes median, box edges encompass 25th to 75th percentiles, whiskers span minimum to maximum values and dots show independent data points.

(Extended Data Fig. 4f). On the basis of previous work showing that efferocytic phagocytes could provide many beneficial factors to dampen inflammation[2,3], we tested whether co-administering early-stage apoptotic cells together with erastin might be of benefit. Notably, single administration of apoptotic cells to the wound site at day 0 along with erastin at day 0 and day 2 (hereafter referred to as the ‘erastin regimen’) markedly accelerated wound healing (Fig. 2g, Extended Data Fig. 4e), with faster and complete closure of initial wounds (Fig. 2h). Mice treated with the erastin regimen reached 50% wound closure at day 4, nearly 2 full days earlier than their respective controls (Fig. 2g).

Of note, administering apoptotic cells alone without erastin did not improve wound closure (Extended Data Fig. 4f). The erastin regimen also greatly decreased the apoptotic cell burden in the wound with fewer cleaved caspase-3^+ cells (even after co-administering apoptotic cells) (Fig. 2i). Thus, the accelerated wound healing required a bolus of early-stage apoptotic cells and SLC7A11 inhibition via erastin. This effect was not related to induction of ferroptosis in the skin, as a ferroptosis inducer RSL3[34] (given together with apoptotic cells) did not improve wound healing (Extended Data Fig. 4g). Additionally, the erastin regimen promoted keratinocyte migration at day 4 post-wounding without affecting proliferation of keratinocytes or fibroblasts (Extended Data Fig. 4h–j). To test the erastin regimen on existing wounds, we administered erastin on day 2 to day 4 post-wounding, which also led to faster healing (Fig. 2j).

To complement the above studies with a genetic approach, we tested SLC7A11-knockout (KO) mice (Fig. 2k), which also exhibited accelerated wound healing dynamics, and this also required co-administration of apoptotic cells on day 0 post-wounding. The wound closure in the SLC7A11-KO mice also reached 50% nearly 2 days earlier than in the control mice (Fig. 2g, k). Thus, interfering with SLC7A11 function in the presence of apoptotic cells can accelerate wound healing in the skin.

Glycogen reserves and glycolysis fuel DC efferocytosis

To better understand how loss or inhibition of SLC7A11 synergizes with apoptotic cells, we performed RNA-seq of control and SLC7A11-deficient DCs engulfing apoptotic cells (Fig. 3a). While there was very little difference in basal gene expression between wild-type and SLC7A11-KO DCs, efferocytic SLC7A11-KO DCs had 191 differentially expressed genes (125 upregulated and 66 downregulated) compared with the wild type. These differentially expressed genes were linked to biological processes including metabolism, protein synthesis, mitochondrial and ER function, transcriptional regulation and wound healing (Fig. 3b, Extended Data Fig. 5a). Metabolic function was the most represented transcriptional programme in SLC7A11-KO DCs, and included genes associated with gluconeogenesis[41,42] (*Gpt2*, *Dyrk1b*, *Hlcs* and *Pck2*), diabetes and obesity[43,44] (*Gdf15* and *Pck2*), amino acid synthesis (*Asns* and *Phgdh*), glutamate metabolism (*Aldh18a1*, *Psat1*, *Gpt2* and *Got1*), and lipid metabolism (*Cyb5r1*, *Soat2*, *Acaa1b* and *Cd5l*).

In macrophages, aerobic glycolysis of glucose is critical for the initial efferocytosis as well as the continued uptake of additional apoptotic corpses[17]. DCs have a unique feature among phagocytes in that they possess intracellular glycogen reserves[45]; genes related to gluconeogenesis were among the top hits in the RNA-seq of SLC7A11-deficient efferocytic DCs. We therefore considered whether SLC7A11-deficient DCs might have increased capacity to convert some of their glycogen reserves to generate more glucose to fuel aerobic glycolysis and thereby promote increased efferocytosis. We compared glycogen reserves between control and SLC7A11-deficient DCs, as well as wild-type DCs before and after erastin treatment. Both SLC7A11-deficient BMDCs and erastin-treated wild-type cDC1s showed reduced intracellular glycogen (Fig. 3c). Addition of the glycogen phosphorylase inhibitor CP-91149 reversed glycogen levels in erastin-treated BMDCs to almost the same level as in the DMSO control (Fig. 3d). Addition of CP-91149 also strongly abrogated the erastin-dependent increase in efferocytosis (Fig. 3d), supporting the notion that glycogenolysis contributes to greater DC efferocytosis. We used two additional approaches to validate a role for glycogenolysis in fuelling enhanced efferocytosis in DCs with inhibition or knockout of SLC7A11. First, siRNA-mediated knockdown of *Pygl*, which encodes glycogen phosphorylase involved in glycogen breakdown, mitigated the increased efferocytosis after SLC7A11 inhibition in BMDCs (Extended Data Fig. 6a, b), although *Pygl* gene expression per se was unaffected by SLC7A11 inhibition (Extended Data Fig. 6e, f). Second, another inhibitor of glycogen phosphorylase (1,4-dideoxy-1,4-imino-D-arabinitol (DAB)) also strongly abrogated increased efferocytosis by DCs with inhibition (Extended Data Fig. 6c) or knockout (Extended Data Fig. 6d) of SLC7A11. Collectively, these data confirm the contribution of glycogen breakdown to increased DC efferocytosis after SLC7A11 inhibition.

We also assessed the role of the rate-limiting enzyme glycogen synthase (GYS1), which affects glycogen synthesis. Erastin treatment increased levels of GYS1 protein, although the inhibitory phosphorylation on GYS1 Ser641, Ser645 and Ser649 by glycogen synthase kinase-3β also increased after erastin treatment. Thus, although there may be more GYS1 protein after erastin treatment, it might be in an inhibitory state and may not promote glycogen synthesis (Extended Data Fig. 6a, e, f). Further, the amount of α-glucosidase (AGL), the debranching enzyme involved in glycogen degradation, was increased after erastin treatment (Extended Data Fig. 6a, e, f). Thus, the depleted glycogen pools in DCs deficient in SLC7A11 or with SLC7A11 inhibition might be the result of alterations in both synthesis and degradation of glycogen.

Next, we tested whether aerobic glycolysis was important for efferocytosis by DCs. Seahorse analysis showed that steady-state SLC7A11-deficient or erastin-treated DCs exhibited increased aerobic glycolysis (ECAR) and a decreased oxygen consumption rate (OCR) (suggestive of mitochondrial oxidative phosphorylation), along with a significantly reduced spare respiratory capacity (Extended Data Fig. 7a, b). During efferocytosis, both wild-type and erastin-treated DCs showed higher aerobic glycolysis and lower OCR (Extended Data Fig. 7a). To validate the influence of SLC7A11 inhibition on glycolysis, we performed a glycolysis stress test on BMDCs in the presence or absence of apoptotic targets and erastin treatment after glucose starvation. The increased glycolytic rate in SLC7A11-KO BMDCs was further augmented during efferocytosis (Fig. 3e, middle). Of note, the increased glycolysis was of a similar magnitude between SLC7A11-KO and erastin-treated wild-type BMDCs (Fig. 3e, right). Although the glycolytic rate was increased in wild-type BMDCs exposed to either apoptotic cells or erastin (Fig. 3e, left), combining erastin with apoptotic cells did not further increase ECAR in wild-type DCs. Collectively, these results suggest that SLC7A11-KO or erastin-treated DCs increase the glycolysis rate to meet the bioenergetic demands of efferocytosis.

To test whether aerobic glycolysis has a role in the enhanced efferocytosis by SLC7A11-deficient DCs, we used several pharmacological inhibitors. The non-metabolizable glucose analogue 2-deoxy-D-glucose (2-DG) abrogated the enhanced efferocytosis due to SLC7A11 inhibition (Fig. 3f). The cell-permeable inhibitor of hexokinase II-mediated glycolysis, 3-bromo-2-oxopropionic acid (3-BP), also dampened the erastin effect (Fig. 3f). SLC7A11-inhibited DCs did not appear to be capable of using alternative fuel substrates such as glutamine or pyruvate (Extended Data Fig. 7d). Similarly, reducing glutamate levels with the glutaminase inhibitor CB-839 did not lead to increased efferocytosis (Extended Data Fig. 7d). Of note, none of the inhibitors interfered with DC viability (Extended Data Fig. 7c). These data suggest that the conversion of glycogen stores in DCs to glucose and the subsequent aerobic glycolysis promote enhanced efferocytosis by SLC7A11-deficient DCs. Notably, co-administration of CP-91149 or 3-BP in the erastin regimen reversed the accelerated wound healing in vivo (Extended Data Fig. 8), linking glycolysis and glycogen dynamics with efferocytosis in cutaneous wound healing.

We then performed targeted metabolomic profiling of the cell pellets from DCs lacking SLC7A11, DCs with SLC7A11 inhibition and control DCs at steady state and during efferocytosis (Extended Data Fig. 9). First, SLC7A11-KO and erastin-treated DCs had similar amounts of cellular cysteine (~50% reduction) compared with controls, confirming the role of SLC7A11. Second, at the steady state, SLC7A11-KO and erastin-treated DCs had similar serine levels, which increased upon efferocytosis (perhaps derived from the ingested corpse). Third, the levels of other amino acids such as lysine, histidine, asparagine and alanine at steady state in DCs were unaffected by knockout or inhibition of SLC7A11; however, the levels of these amino acids increased (irrespective of the genotype) in efferocytic DCs, probably owing to the apoptotic cargo. Further,

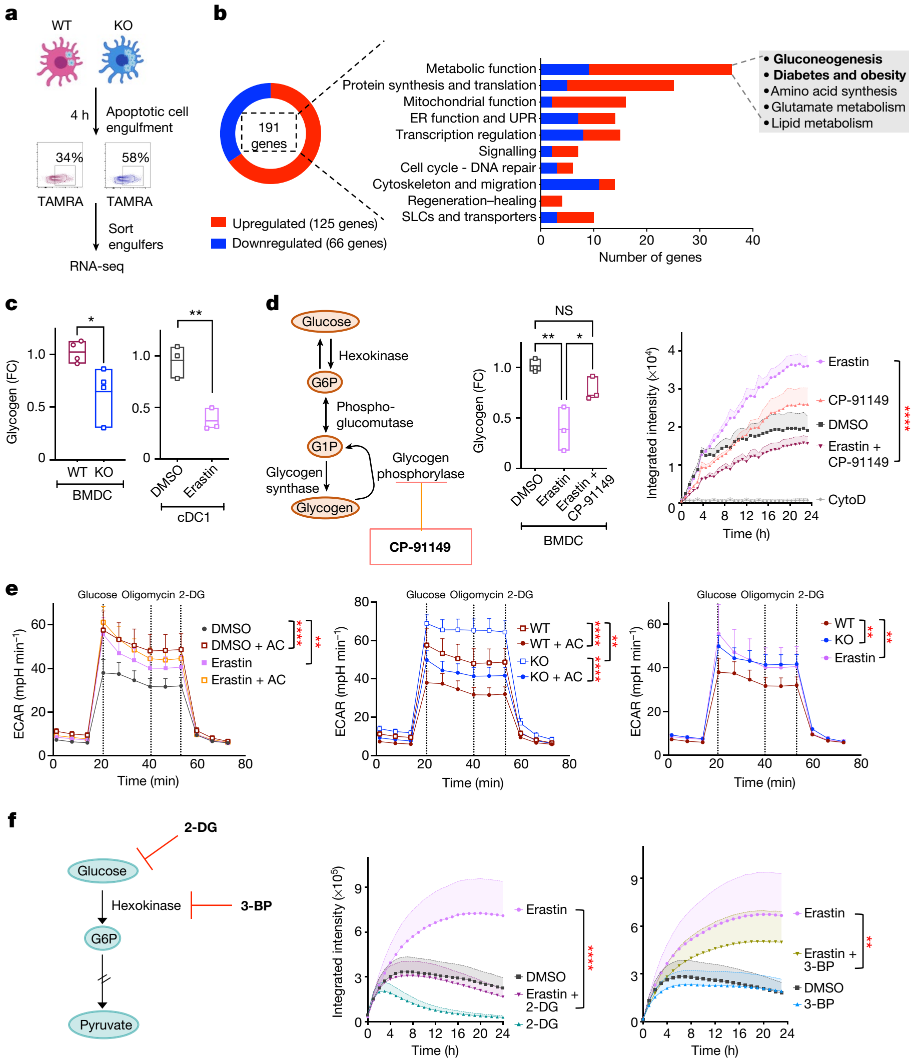

Fig. 3 | Glycolysis and glycogen reserves fuel enhanced efferocytosis. **a**, Schematic of RNA-seq analysis of SLC7A11-deficient BMDCs engulfing TAMRA-labelled apoptotic cells for 4 h. TAMRA$^+$ phagocytes (engulfers) were sorted directly into lysis buffer for RNA-seq analysis. The contour plots represent one of four independent experiments. **b**, Pathway analysis of differentially expressed genes regulated in efferocytic SLC7A11-KO versus wild-type DCs. Data are from three to four independent experimental replicates. **c**, Glycogen levels in lysates of DC populations from vehicle- or erastin-treated wild-type mice (right), or untreated wild-type or SLC7A11-KO mice (left). *n* = 4 (BMDC), *n* = 3 (cDC1). Unpaired two-tailed *t*-test. Results are presented as fold change (FC). **d**, Schematic of glycogen metabolism pathway (left). Effect on glycogen levels in BMDCs treated with erastin or CP-91149 or both (middle; *n* = 3 per condition; one-way ANOVA with Tukey's multiple comparisons test). Right, kinetics of efferocytosis after erastin (*n* = 5) or combined erastin and CP-91149 (*n* = 5) treatment. DMSO (vehicle; *n* = 5 per condition) and CytoD (as negative control; *n* = 3) are also shown. **e**, Increased glycolytic function in DCs during apoptotic cell clearance and SLC7A11 inhibition. Glycolysis was measured in wild-type versus SLC7A11-KO and vehicle or erastin-inhibited DCs at steady state or during efferocytosis. Data are mean ± s.e.m. of *n* = 3 per group. Two-way ANOVA with Tukey's multiple comparisons test. AC, apoptotic cells. **f**, Left, schematic of aerobic glycolysis pathway showing targets of inhibitors. Right, kinetics of efferocytosis by BMDCs treated with indicated inhibitors (left, *n* = 4; right, *n* = 5). Floating bars (**c**, **d**) show the range of values, dots represent independent replicates and the line denotes the mean. All live-cell imaging data (**d**, **f**) are expressed as mean ± s.e.m.; one-way ANOVA with Tukey's multiple comparisons test.

targeting the synthesis of serine from glucose (via PHGDH, PSAT1 and PSPH) and the synthesis of cysteine from serine (via CTH)—either by siRNA targeting or by pharmacological inhibition—did not alter efferocytosis by control DCs or enhanced efferocytosis by erastin-treated DCs (data not shown). Collectively, these data suggest that serine—a precursor of cysteine—or other amino acids do not appear to contribute to the enhanced efferocytosis in SLC7A11-inhibited DCs.

SLC7A11 and wound healing in diabetic mice

Non-healing chronic wounds are a serious complication affecting the quality of life in patients with diabetes[46]. To test the relevance of SLC7A11 for wound healing in diabetes (hereafter referred to as diabetic wound healing), we used leptin receptor-deficient *db/db* mice, which represent a model of human type 2 diabetes with obesity and hyperglycemia. As expected, the skin excision model showed that wound healing is impaired in *db/db* mice, with a delay of nearly three days to reach half-maximal closure (Fig. 4a and ref. [46]). *Slc7a11* expression was 200-fold higher on day 4 in the wounds of *db/db* mice compared with normoglycaemic C57BL/6 mice (Fig. 4b). To test whether SLC7A11 inhibition might affect diabetic wound healing, we treated *db/db* mice after wounding with erastin alone or with the erastin regimen (with co-administration of apoptotic cells). Diabetic wounds treated with erastin alone exhibited accelerated closure, probably because there were enough uncleared apoptotic cells in the diabetic wounds (Fig. 4c). Wounds of C57BL/6 mice contained up to around 400 apoptotic cells

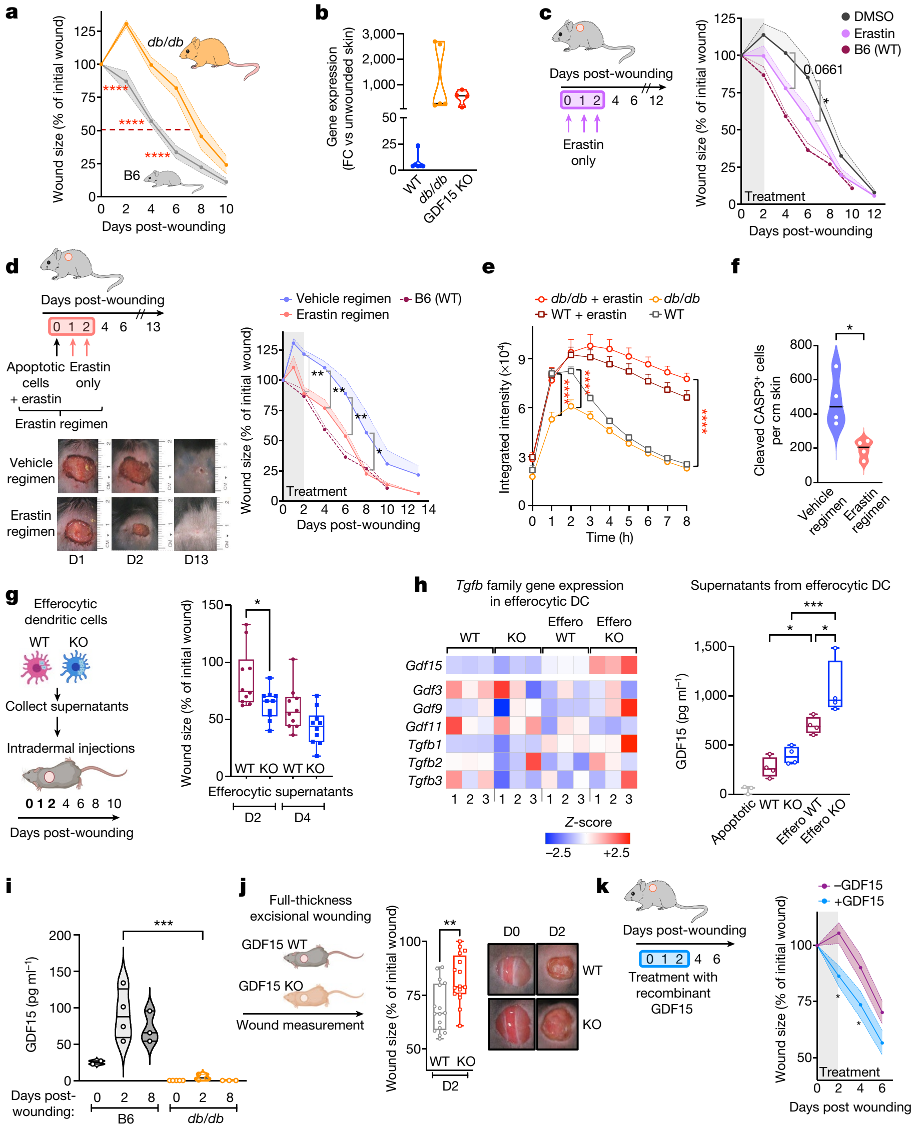

Fig. 4 | SLC7A11 inhibition and GDF15 promote wound healing in skin of diabetic mice. a, Delayed healing in diabetic mice (*n* = 11 (*db/db*); *n* = 8 (B6)). **b**, *Slc7a11* expression in skin lysates from unwounded and wounded (day 4 after wounding) wild-type (*n* = 6), *db/db* (*n* = 5), and GDF15-KO (*n* = 5) mice. **c**, **d**, Erastin alone (**c**) and erastin regimen (**d**) accelerate diabetic wound healing. **c**, *db/db* mice were treated with erastin (*n* = 8) or DMSO (*n* = 7). **d**, *db/db* mice were treated with the erastin regimen (*n* = 8) or DMSO (*n* = 7). Wound healing of normoglycaemic (B6) mice is also shown (*n* = 8). Data represent one of three independent experiments. **e**, Erastin enhances efferocytosis in DCs from diabetic mice. Data are mean ± s.e.m. *n* = 7 (WT and *db/db* DMSO), *n* = 4 (WT and *db/db* erastin). One-way ANOVA with Tukey's multiple comparisons (*db/db* DMSO versus erastin; all time points); two-way ANOVA with Sidak's multiple comparisons for WT versus *db/db* DCs (time points 1 h and 2 h). **f**, Apoptotic cell load in diabetic wounds (*n* = 4 per group) (**P* = 0.0124; unpaired two-tailed *t*-test). **g**, Healing dynamics of wild-type mice (*n* = 10 per group) treated with supernatants from efferocytic SLC7A11-KO and wild-type DCs. **h**, Left, heat map of TGFβ superfamily genes. Data are presented as *z*-score from three independent experimental replicates. Right, GDF15 secretion by DCs 12 h after incubation with apoptotic targets (*n* = 4 per condition) or by the targets alone (*n* = 3). Effero, efferocytic cells. **i**, GDF15 levels in lysates from unwounded (*n* = 2 (B6), *n* = 5 (*db/db*)) and wounded skin (*n* = 3–4 (B6), *n* = 3 (*db/db*)). **j**, Wound size in GDF15-KO and littermate control mice (*n* = 16 per group; unpaired two-tailed *t*-test). **k**, Topical administration of recombinant GDF15 improves diabetic wound healing. *n* = 11. **a**, **c**, **d**, **g**, **k**, Data are mean ± s.e.m.; two-way ANOVA with multiple comparisons. **h**, **i**, one-way ANOVA with Tukey's multiple comparisons test. Violin plots (**b**, **f**, **i**) show the entire range of values and the centre line denotes the median, with dots representing independent replicates. In box plots (**g**, **h**, **j**), the centre line denotes median, box edges encompass 25th to 75th percentiles, whiskers span minimum to maximum values and dots show independent data points.

(cells positive for cleaved caspase-3) on day 4 after wounding (Fig. 2i) and around 50 apoptotic cells on day 13, whereas those in diabetic mice still had around 400 apoptotic cells on day 13 (Fig. 4c), reflecting the increased apoptotic load. The erastin regimen improved healing in the *db/db* mice as early as day 2 after wounding, continuing to full closure by day 13, and reaching 50% closure of the initial wound 2–3 days earlier than in untreated *db/db* mice (Fig. 4d).

Next, we tested the link between efferocytosis and the accelerated wound closure in the *db/db* mice. In ex vivo analysis, DCs from *db/db* mice showed reduced efferocytosis compared with those from wild-type mice, with a more pronounced difference at earlier time points (Fig. 4e) (analogous to macrophages from diabetic mice[13]). Notably, erastin rescued the defective efferocytosis of DCs from *db/db* mice (Fig. 4e). Consistent with this ex vivo phenotype, the erastin regimen substantially reduced uncleared apoptotic cells in the wounds of *db/db* mice (Fig. 4f). Whereas erastin reduces the apoptotic cell burden with or without an apoptotic cell bolus in the *db/db* mice, the apoptotic cell burden in the control C57BL/6 mice was reduced only with the erastin regimen. Although there was an overall lower apoptotic cell burden in the wounds of control mice compared to diabetic mice, the addition of the apoptotic bolus promoted the effect of erastin (Extended Data Fig. 10a, b).

As the combination of SLC7A11 inhibition together with apoptotic cell addition to the wounds provided the most efficient wound healing, and efferocytic phagocytes secrete factors that are known to provide beneficial effects in tissues[47], we tested whether secreted factors from efferocytic SLC7A11-deficient DCs contributed to the accelerated healing. We purified supernatants from efferocytic wild-type and SLC7A11-KO DCs and added these exogenous supernatants to the excision wounds. Mice treated with efferocytic supernatants from efferocytic SLC7A11-deficient DCs exhibited faster wound closure compared with those treated with supernatants from wild-type DCs (Fig. 4g).

Soluble factors, including members of TGFβ superfamily (TGFβ1, TGFβ2 and TGFβ3) are released by efferocytic phagocytes and can affect wound healing[48]. Mining the transcriptome of efferocytic SLC7A11-deficient DCs, we noted upregulation of *Gdf15*, which encodes growth differentiation factor 15 (Fig. 4h), a member of the TGFβ superfamily. GDF15 has been associated with obesity, diabetes, cancer, cardiovascular, kidney disorders and tissue regeneration[43,49,50]. The amount of GDF15 protein was significantly increased in the supernatants of efferocytic DCs from SLC7A11-deficient mice compared with wild-type littermates (Fig. 4h). GDF15 levels increased (two- to fivefold) at day 2 after excisional skin wounding compared with unwounded skin and remained high even at later stages of healing (day 8) (Fig. 4i). When we tested GDF15-deficient mice with the excisional skin biopsy model, they displayed larger wounds on day 2 compared with littermate control mice (Fig. 4j), and this correlated with increased *Slc7a11* expression in the wounds (Fig. 4b). Consistent with the notion that GDF15 is produced downstream of efferocytosis, GDF15-deficient DCs showed similar *Slc7a11* expression at the steady state (Extended Data Fig. 10c) and similar efferocytosis (Extended Data Fig. 10d) to control DCs. When we treated GDF15-KO mice with erastin, we detected a partial enhancement in wound closure compared with vehicle (Extended Data Fig. 10e), indicating GDF15-dependent as well as GDF15-independent effects of SLC7A11 blockade in wound healing.

Of note, GDF15 is almost undetectable in the wounds of *db/db* mice compared with normoglycaemic (B6) mice (Fig. 4i). We therefore tested whether recombinant GDF15 promoted wound healing in *db/db* mice; application of rGDF15 significantly improved wound healing (Fig. 4k). These data suggest that reduced efferocytosis and lower GDF15 levels, both of which correlate with high SLC7A11 expression in the diabetes-prone mice, contribute to delayed skin wound healing. Thus, SLC7A11 inhibition at the wound site can improve diabetic wound healing through at least two modalities: improving cell clearance and via factors such as GDF15 from the efferocytic cells that promote wound healing.

Discussion

Here we have used in vitro, ex vivo and in vivo approaches and metabolomics to investigate DC-mediated efferocytosis and tissue regeneration/wound healing. First, we observe that expression of multiple membrane proteins and transporters is modulated during apoptotic cell engulfment by DCs, including the amino acid transporter SLC7A11, which acts as a negative regulator of efferocytosis. It is unclear why this negative regulator of efferocytosis would be upregulated following wounding, although concurrent upregulation of negative and positive regulators (that is, simultaneous acceleration and braking) is probably part of a finely balanced signalling regulation in vivo, as has been observed in T cells during antigen receptor signalling, in fibroblasts during growth factor stimulation, and in macrophages during FcR-mediated phagocytosis. Mechanistically, the enhanced efferocytosis in SLC7A11-deficient DCs is fuelled in part by increased aerobic glycolysis, in which glucose is derived from glycogen stores, a unique feature of DCs among phagocytes. We also reveal DCs as participants in clearing apoptotic cells during cutaneous skin injury. Notably, the combination of SLC7A11 blockade together with apoptotic cells improves wound healing kinetics. This accelerated wound healing is observed in both wild-type mice and in diabetes-prone *db/db* mice. Transcriptomic analysis of SLC7A11-deficient DCs identified GDF15 as a key extracellular mediator that is released from efferocytic DCs and facilitates wound closure downstream of SLC7A11. In sum, starting from unbiased transcriptomic analysis of efferocytic DCs, we have identified SLC7A11 as a brake on DC phagocytosis and outlined an approach to improve cutaneous wound healing using inhibition of SLC7A11. This strategy could be relevant for management of wounds in diabetes and other skin conditions associated with chronic inflammation.

Online content

Any methods, additional references, Nature Research reporting summaries, source data, extended data, supplementary information, acknowledgements, peer review information; details of author contributions and competing interests; and statements of data and code availability are available at https://doi.org/10.1038/s41586-022-04754-6.

1. Henson, P. M. Cell removal: efferocytosis. *Annu. Rev. Cell Dev. Biol.* **33**, 127–144 (2017).
2. Boada-Romero, E., Martinez, J., Heckmann, B. L. & Green, D. R. The clearance of dead cells by efferocytosis. *Nat. Rev. Mol. Cell Biol.* **21**, 398–414 (2020).
3. Morioka, S., Maueroder, C. & Ravichandran, K. S. Living on the edge: efferocytosis at the interface of homeostasis and pathology. *Immunity* **50**, 1149–1162 (2019).
4. Cabeza-Cabrerizo, M., Cardoso, A., Minutti, C. M., Pereira da Costa, M. & Reis, E. S. C. Dendritic cells revisited. *Annu. Rev. Immunol.* **39**, 131–166 (2021).
5. Guermonprez, P. & Amigorena, S. Pathways for antigen cross presentation. *Springer Semin. Immunopathol.* **26**, 257–271 (2005).
6. Albert, M. L., Sauter, B. & Bhardwaj, N. Dendritic cells acquire antigen from apoptotic cells and induce class I-restricted CTLs. *Nature* **392**, 86–89 (1998).
7. Gallucci, S., Lolkema, M. & Matzinger, P. Natural adjuvants: endogenous activators of dendritic cells. *Nat. Med.* **5**, 1249–1255 (1999).
8. Blander, J. M. & Medzhitov, R. On regulation of phagosome maturation and antigen presentation. *Nat. Immunol.* **7**, 1029–1035 (2006).
9. Khanna, S. et al. Macrophage dysfunction impairs resolution of inflammation in the wounds of diabetic mice. *PLoS ONE* **5**, e9539 (2010).
10. Wetzler, C., Kampfer, H., Stallmeyer, B., Pfeilschifter, J. & Frank, S. Large and sustained induction of chemokines during impaired wound healing in the genetically diabetic mouse: prolonged persistence of neutrophils and macrophages during the late phase of repair. *J. Invest. Dermatol.* **115**, 245–253 (2000).
11. Moulik, P. K., Mtonga, R. & Gill, G. V. Amputation and mortality in new-onset diabetic foot ulcers stratified by etiology. *Diabetes Care* **26**, 491–494 (2003).
12. Lenz, A., Heine, M., Schuler, G. & Romani, N. Human and murine dermis contain dendritic cells. Isolation by means of a novel method and phenotypical and functional characterization. *J. Clin. Invest.* **92**, 2587–2596 (1993).
13. Seneschal, J., Clark, R. A., Gehad, A., Baecher-Allan, C. M. & Kupper, T. S. Human epidermal Langerhans cells maintain immune homeostasis in skin by activating skin resident regulatory T cells. *Immunity* **36**, 873–884 (2012).
14. Mirza, R., DiPietro, L. A. & Koh, T. J. Selective and specific macrophage ablation is detrimental to wound healing in mice. *Am. J. Pathol.* **175**, 2454–2462 (2009).
15. Shook, B., Xiao, E., Kumamoto, Y., Iwasaki, A. & Horsley, V. CD301b$^+$ macrophages are essential for effective skin wound healing. *J. Invest. Dermatol.* **136**, 1885–1891 (2016).
16. Phillipson, M. & Kubes, P. The healing power of neutrophils. *Trends Immunol.* **40**, 635–647 (2019).
17. Morioka, S. et al. Efferocytosis induces a novel SLC program to promote glucose uptake and lactate release. *Nature* **563**, 714–718 (2018).
18. Kelly, B. & Pearce, E. L. Amino assets: how amino acids support immunity. *Cell Metab.* **32**, 154–175 (2020).
19. Procaccini, C. et al. Signals of pseudo-starvation unveil the amino acid transporter SLC7A11 as key determinant in the control of T_{reg} cell proliferative potential. *Immunity* **54**, 1543–1560.e6 (2021).
20. D'Angelo, J. A. et al. The cystine/glutamate antiporter regulates dendritic cell differentiation and antigen presentation. *J. Immunol.* **185**, 3217–3226 (2010).
21. Fotiadis, D., Kanai, Y. & Palacin, M. The SLC3 and SLC7 families of amino acid transporters. *Mol. Aspects Med.* **34**, 139–158 (2013).
22. Merckx, E. et al. Absence of system x_c^- on immune cells invading the central nervous system alleviates experimental autoimmune encephalitis. *J. Neuroinflammation* **14**, 9 (2017).

23. Massie, A. et al. Time-dependent changes in striatal xCT protein expression in hemi-Parkinson rats. *Neuroreport* **19**, 1589–1592 (2008).
24. Mesci, P. et al. System x_C^- is a mediator of microglial function and its deletion slows symptoms in amyotrophic lateral sclerosis mice. *Brain* **138**, 53–68 (2015).
25. Lin, C. H. et al. Decreased mRNA expression for the two subunits of system x_c^-, SLC3A2 and SLC7A11, in WBC in patients with schizophrenia: Evidence in support of the hypo-glutamatergic hypothesis of schizophrenia. *J. Psychiatr. Res.* **72**, 58–63 (2016).
26. Massie, A. et al. Dopaminergic neurons of system x_c^--deficient mice are highly protected against 6-hydroxydopamine-induced toxicity. *FASEB J.* **25**, 1359–1369 (2011).
27. Kaleeba, J. A. & Berger, E. A. Kaposi's sarcoma-associated herpesvirus fusion-entry receptor: cystine transporter xCT. *Science* **311**, 1921–1924 (2006).
28. Kandasamy, R. K. et al. A time-resolved molecular map of the macrophage response to VSV infection. *NPJ Syst. Biol. Appl.* **2**, 16027 (2016).
29. Rabinowitz, J. et al. xCT/SLC7A11 antiporter function inhibits HIV-1 infection. *Virology* **556**, 149–160 (2021).
30. Robert, S. M. et al. SLC7A11 expression is associated with seizures and predicts poor survival in patients with malignant glioma. *Sci. Transl. Med.* **7**, 289ra286 (2015).
31. Koppula, P., Zhuang, L. & Gan, B. Cystine transporter SLC7A11/xCT in cancer: ferroptosis, nutrient dependency, and cancer therapy. Protein Cell https://doi.org/10.1007/s13238-020-00789-5 (2020).
32. Hassannia, B., Vandenabeele, P. & Vanden Berghe, T. Targeting ferroptosis to iron out cancer. *Cancer Cell* **35**, 830–849 (2019).
33. Conrad, M. & Pratt, D. A. The chemical basis of ferroptosis. *Nat. Chem. Biol.* **15**, 1137–1147 (2019).
34. Jiang, X., Stockwell, B. R. & Conrad, M. Ferroptosis: mechanisms, biology and role in disease. *Nat. Rev. Mol. Cell Biol.* **22**, 266–282 (2021).
35. Zilka, O. et al. On the mechanism of cytoprotection by ferrostatin-1 and liproxstatin-1 and the role of lipid peroxidation in ferroptotic cell death. *ACS Cent. Sci.* **3**, 232–243 (2017).
36. Sato, M. et al. The ferroptosis inducer erastin irreversibly inhibits system x_c^- and synergizes with cisplatin to increase cisplatin's cytotoxicity in cancer cells. *Sci. Rep.* **8**, 968 (2018).
37. Rajesh, A. et al. Depletion of langerin$^+$ cells enhances cutaneous wound healing. *Immunology* **160**, 366–381 (2020).
38. Rajesh, A. et al. Skin antigen-presenting cells and wound healing: new knowledge gained and challenges encountered using mouse depletion models. *Immunology* **163**, 98–104 (2021).
39. Lachmann, A. et al. Massive mining of publicly available RNA-seq data from human and mouse. *Nat. Commun.* **9**, 1366 (2018).
40. Zhang, Y. et al. Imidazole ketone erastin induces ferroptosis and slows tumor growth in a mouse lymphoma model. *Cell Chem. Biol.* **26**, 623–633.e629 (2019).
41. Keramati, A. R. et al. A form of the metabolic syndrome associated with mutations in *DYRK1B*. *N. Engl. J. Med.* **370**, 1909–1919 (2014).
42. Honma, K., Kamikubo, M., Mochizuki, K. & Goda, T. Insulin-induced inhibition of gluconeogenesis genes, including glutamic pyruvic transaminase 2, is associated with reduced histone acetylation in a human liver cell line. *Metabolism* **71**, 118–124 (2017).
43. Nakayasu, E. S. et al. Comprehensive proteomics analysis of stressed human islets identifies GDF15 as a target for type 1 diabetes intervention. *Cell Metab.* **31**, 363–374.e366 (2020).
44. Beale, E. G., Harvey, B. J. & Forest, C. PCK1 and PCK2 as candidate diabetes and obesity genes. *Cell Biochem. Biophys.* **48**, 89–95 (2007).
45. Thwe, P. M. et al. Cell-intrinsic glycogen metabolism supports early glycolytic reprogramming required for dendritic cell immune responses. *Cell Metab.* **26**, 558–567.e555 (2017).
46. Zhao, G. et al. Delayed wound healing in diabetic (*db/db*) mice with *Pseudomonas aeruginosa* biofilm challenge: a model for the study of chronic wounds. *Wound Repair Regen.* **18**, 467–477 (2010).
47. Bonnefoy, F. et al. Factors produced by macrophages eliminating apoptotic cells demonstrate pro-resolutive properties and terminate ongoing inflammation. *Front. Immunol.* **9**, 2586 (2018).
48. Pakyari, M., Farrokhi, A., Maharlooei, M. K. & Ghahary, A. Critical role of transforming growth factor beta in different phases of wound healing. *Adv. Wound Care* **2**, 215–224 (2013).
49. Coll, A. P. et al. GDF15 mediates the effects of metformin on body weight and energy balance. *Nature* **578**, 444–448 (2020).
50. Patsalos, A. et al. A growth factor-expressing macrophage subpopulation orchestrates regenerative inflammation via GDF-15. *J. Exp. Med.* **219**, e20210420 (2021).

Methods

Mouse tissue processing

Cells from ears of SLC7A11-KO and control littermates were isolated as described[51]. In brief, ear skin samples were collected by cutting at the ear base and were incubated overnight at 4 °C with 200 μg ml^{-1} Dispase II (from *Bacillus* polymerase grade 2; Roche) to facilitate manual cutting and isolation of cells. Small skin pieces were further digested with 1.5 mg ml^{-1} collagenase type 4 (Worthington) and 10 U DNase (Roche) in RPMI medium buffered with HEPES and supplemented with 2% fetal calf serum. The suspension was resuspended every 30 min and provided with fresh digestion buffer for a total of 90 min at 37 °C. After digestion, the cell suspension was filtered to remove debris and clots. For spleen single-cell suspensions, spleens were digested in RPMI medium supplemented with 0.01 U ml^{-1} DNase I (Roche) and 0.02 mg ml^{-1} Liberase (Roche) for 30 min. Red blood cells were removed with a 1× solution of RBC lysis buffer (Biolegend, 420301). For bone-marrow progenitors, bone marrow was isolated from femurs and tibia of 8- to 12-week-old mice.

Cell isolation

Single-cell suspensions of digested ears and spleens were further enriched for phagocytes by depleting lymphocyte populations. Depletion was performed using monoclonal biotin-linked antibodies against CD3e (145-2C11, 13-0031-82 eBioscience), CD19 (eBio1D3-1D3, 13-0193-82 eBioscience), NK1.1 (PK136, 13-5941-82 eBioscience) followed by collection of non-depleted cells using MagniSort Streptavidin Negative Selection Beads (MSNB-6002-74 ThermoFisher). BMDCs and macrophages were generated from mice by culturing bone marrow progenitors for 10 days in GM-CSF-supplemented medium and for 6 days in M-CSF-supplemented medium, respectively, and as described[52].

Flow cytometry and cell sorting

Immunophenotyping of mouse skin or spleen was performed on single-cell suspensions. Cells were stained with the following anti-mouse, monoclonal, fluorochrome-linked antibodies: CD24-AF488 or CD24-eFluor450 (1:100; M1/69; 101816 or 48-0242-82, BioLegend), CD11b-BV605 (1:200; M1/70; 563015, BD Biosciences), CD26-FITC or CD26-BV650 (1: 200; H194-112; 559652 or 740474, BioLegend), CD11c-BV711 (1:200; HL3; 563048, BD Biosciences), F4/80-BV785 (1:200; BM8; 123141, BioLegend), CD45-AF700 (1:500; 30-F11; 56-0451-82, ThermoFisher), MHCII (I-A/I-E)-eFluor780 (1:400; M5/114.15.2; 47-5321-82, ThermoFisher), CD172a (SIRPα)-PerCP-eFluor710 (1:200; P84; 46-1721-82, ThermoFisher), CD103-BUV395 (1:200; M290; 740238, BD Biosciences), CD64-BV421 or CD64-PE/Cy7 (1:100; X54-5/7.1; 139309 or 139314, BioLegend), XCR1-BV650 (1:200; ZET; 148220, BioLegend) and Fc receptor-blocking antibody CD16/CD32 (1:300; clone 2.4G2, 553142, BD Biosciences). Viable cells were discriminated using Fixable Viability Dye eFluor 506 (65-0866-18, ThermoFisher). Prior to measuring, counting beads (01-1234-42, ThermoFisher) were added to the cells for some experiments. Measurements were performed on a BD LSR Fortessa cytometer and analysed using FlowJo10 software (Tree Star). Cell sorting was performed on FACS ARIAII and III (BD Biosciences).

Ferroptosis characterization

To assess ferroptosis, we used BODIPY 581/591 (C11-BODIPY) and dihydrorhodamine 123 (DHR123) probes that change their fluorescence properties upon oxidation, as previously described[53]. In brief, DCs were treated with 5 μM erastin (S7242, Bio-Connect) or 1 μM ML-162 (AOB1514) or DMSO control prior to addition of fluorescent probes 1 h before measurement: 0.5 μM C11-BODIPY (D3861, ThermoFisher) or 1 μM DHR-123 (85100, Cayman Chemical) and 0.5 μM of DRAQ7 cell death stain (DR70250, BioStatus).

Determination of glycogen concentration

The glycogen concentration was measured using a Glycogen Colorimetric/Fluorometric Assay Kit (GENT-K646-10, BioVision) according to the manufacturer's instructions.

Determination of glutathione levels

Glutathione was quantified in DCs 2 h after erastin treatment using the GSH/GSSG-Glo Assay luminescence-based system according to the manufacturer's instructions (V6611, Promega). GSH/glutathione disufide (GSSG) ratios were calculated from luminescence measurements (in relative light units (RLU)) and after interpolation of glutathione concentrations from standard curves. Data for both glycogen and glutathione are reported as fold change from DMSO (vehicle)-treated cells or from wild-type cells.

Seahorse analysis

One-hundred thousand BMDCs were seeded on a Seahorse 96-well tissue culture plate (Agilent Technologies). The plate was allowed to stand for 30 min for the cells to settle before placing it in the incubator overnight. The adhered cells were treated with 5 μM erastin (S7242, Bio-Connect) or 200 μM CP-91149 (S2717, Bio-Connect) 2 h prior to Seahorse analysis. The cells were switched to serum-free Seahorse media before the assay according to the manufacturer's instructions. For basal ECAR and OCR, the cells were subjected to XF Real Time ATP Rate kit (103592-100, Agilent Technologies). For assessment of respiratory capacity, cells were subjected to XF Cell Mito Stress Test Kit (103015-100, Agilent Technologies). Oligomycin (1.5 μM), FCCP (1 μM) and rotenone plus antimycin A (0.5 μM) were injected sequentially. For cells subjected to Seahorse XF Glycolysis Stress Test Kit (103020-100, Agilent Technologies), glucose (10 mM), oligomycin (1 mM) and 2-DG (50 mM) were injected sequentially. At the beginning of the assay, the medium was changed to unbuffered, glucose-free DMEM (Sigma-Aldrich Cat D5030, pH 7.35 at 37 °C) supplemented with 2 mM glutamine.

Efferocytosis assays

For induction of apoptosis, human Jurkat T cells were stained with CypHer5E (PA15401, GE Healthcare) or TAMRA (C-1171, Invitrogen) or pHrodo Green STP Ester (P35369, ThermoFisher), resuspended in RPMI with 5% fetal calf serum, treated with 150 mJ cm^{-2} ultraviolet C irradiation (Stratalinker) and incubated for 4 h at 37 °C with 5% CO$_2$. DCs were incubated with apoptotic targets at a 1:5 phagocyte:target ratio for the indicated times. Phagocytosis was assessed by a flow cytometry-based assay or by Incucyte Live-cell imaging. As alternative targets for phagocytosis, DCs were incubated with pHrodo Green *E. coli* BioParticles (P35366, ThermoFisher) or Streptavidin Fluoresbrite YG Microspheres, 2.0 μm (beads) at a 1:5 phagocyte:target ratio for the indicated times. When applicable, cells were pretreated for 1 h with 5 μM erastin (S7242, Bio-Connect), 200 μM CP-91149 (S2717, Bio-Connect), 0.2 mM 2-DG (D8375-1G, Sigma), 5 μM UK5099 (PZ0160, Sigma), 40 μM 6-diazo-5-oxo-L-norleucine (DON) (D2141-5MG, Sigma), 10 μM 3-BP (376817-M, Sigma), 10 mM glutamate (6106-04-3, Sigma), 0.5 μM ferrostatin-1(S7243, Bio-Connect), 1 μM FCCP (HY-100410, Bio-Connect), 100 μM MitoTEMPO (SML0737, Sigma), 1–2 μM L-GSH (G4251-10G, Sigma), 50 μM L-buthionine-(*S*,*R*)-sulfoximine (BSO) (S9728, Bio-Connect), 1 mM DAB (20939-5, Cayman Chemical) and 2 μM CB-839 (S7655, Bio-Connect) before addition of targets.

siRNA experiments

DCs were treated with SMARTpool: Accell *Slc7a11* siRNA (E-047420-00-0010), Accell *Slc7a1* siRNA (E-042922-00-0005), Accell *Slc7a5* siRNA (E-041166-00-0010), Accell *Pygl* siRNA (E-046873-00-0005) or Accell non-targeting siRNA #1 (D-001910-01-05) and Accell non-targeting siRNA #4 (D-001910-04-05) (Dharmacon) according to the manufacturer's instructions, two days before the engulfment assay.

RT–qPCR

Total RNA was extracted from cells using the RNeasy Mini Kit (Qiagen) and cDNA was synthesized using Sensifast cDNA Synthesis Kit (BIO-650504), according to the manufacturer's instructions. Quantitative gene expression analysis for mouse genes was performed using mouse-sequence specific Taqman probes that are non-cross reactive with human sequences (Applied Biosystems), run on a Roche Lightcycler 480 -384.

ELISA

GDF15 levels were measured in supernatants of DCs or total skin lysates by using Mouse/Rat GDF15 Quantikine ELISA Kit (MGD150, R&D Systems). For skin lysates, shaved skin was lysed in 50 mM Tris–HCl (pH 8.5) using the Precellys 24 tissue homogenizer and 25 µg lysate per sample was used for ELISA.

RNA sequencing

Wild-type or SLC7A11-deficient BMDCs were co-cultured with apoptotic Jurkat cells for 4 h, unbound Jurkat cells were removed by washing with PBS and engulfing BMDCs were isolated by sorting with BD FACSAriaIII Cell Sorter. Total RNA was extracted, and an mRNA library was prepared using the Illumina Novoseq 6000 platform (Novogene). HISAT2 was selected to map the filtered sequenced reads to the reference genome. BAM files containing mapping results were counted using the feature counts function in the R package Rsubread. Counting was performed using both mouse and human genomes for comparison although downstream analyses were only performed on mouse data. Differentially expressed genes analysis was then performed using DESeq2 considering all genes with FDR ≤ 0.05 and $0.58 \le \log_2(\text{fold change}) \le -0.58$. All genes that resulted from the analysis were curated using multiple methods, including literature mining and function determination (known or predicted) via UniProt.

scRNA-seq and analysis

scRNA-seq datasets on live cells sorted from control wild-type (WT: Cre-negative *Otulin*$^{fl/fl}$; $n = 1$) skin and lesional (L; $n = 3$) and non-lesional (NL; $n = 2$) Δ^{Ker}OTULIN skin are fully described in ref. [54].

Bioinformatics analysis

Gene sets were tested for unidirectional enrichment and visualized using the Triwise package. Proximity represents upregulation in more than one population, and the distance from the origin represents the strength of expression. Gene expression datasets analysed in RStudio Version 1.2.1335 and based on mean values of the normalized gene counts of each of three DC populations (lung, skin and spleen) extracted from ImmGen Microarray V1 dataset GSE15907.

Targeted metabolomics

Metabolite extracts have been analysed by either reverse phase chromatography or hydrophilic interaction chromatography (HILIC). For reverse phase chromatography, metabolite extracts have been dried down and resolved in an equal volume of 0.1% formic acid in water. One microlitre of this extract has been separated on a Kinetex (Phenomenex) C18 column (100 Å, 150 × 2.1 mm) connected with the respective guard column, employing a 7-min-long linear gradient from 99% A (1 % acetonitrile, 0.1 % formic acid in water) to 60% B (0.1 % formic acid in acetonitrile) at a flow rate of 80 µl min^{-1}. UV detection was used for quality control only. Detection and quantification was done by on-line tandem mass spectrometry (LC–MS/MS) using the selected reaction monitoring (SRM) mode of a TSQ Altis mass spectrometer (Thermo Fisher Scientific), using the following transitions in the positive ion mode: 147 *m/z* to 84 *m/z* (lysine), 156 *m/z* to 110 *m/z* (histidine), 175 *m/z* to 70 *m/z* (arginine), 223 *m/z* to 88 *m/z* (cystathionine), 241 *m/z* to 74 *m/z* (cystine), 399 *m/z* to 250 *m/z* (*S*-adenosyl methionine), 76 *m/z* to 30 *m/z* (glycine), 106 *m/z* to 60 *m/z* (serine), 133 *m/z* to 74 *m/z* (asparagine), 134 *m/z* to 74 *m/z* (aspartic acid), 147 *m/z* to 130 *m/z* (glutamine), 148 *m/z* to 84 *m/z* (glutamic acid), 90 *m/z* to 44 *m/z* (alanine), 120 *m/z* to 74 *m/z* (threonine), 122 *m/z* to 76 *m/z* (cysteine), 116 *m/z* to 70 *m/z* (proline), 118 *m/z* to 72 *m/z* (valine), 150 *m/z* to 133 *m/z* (methionine), 132 *m/z* to 86 *m/z* (leucine and isoleucine), 182 *m/z* to 36 *m/z* (tyrosine), 385 *m/z* to 136 *m/z* (*S*-adenosyl-homocysteine), 166 *m/z* to 133 *m/z* (phenylalanine), 298 *m/z* to 136 *m/z* (5′-methylthioadenosine) and 205 *m/z* to 188 *m/z* (tryptophan). In an independent analysis, 1 µl of the original sample was injected onto a polymeric iHILIC-(P) Classic HPLC column (HILICON, 100 × 2.1 mm; 5 µm) and the respective guard column, operated at a flow rate of 100 µl min^{-1}. The HPLC (Ultimate 3000 HPLC system; Dionex, Thermo Fisher Scientific) was directly coupled via electrospray ionization to a TSQ Quantiva mass spectrometer (Thermo Fisher Scientific). A linear gradient (A: 95% acetonitrile 5%, 10 mM aqueous ammonium acetate; B: 5 mM aqueous ammonium bicarbonate) starting with 15% B and ramping up to 60% B in 9 min was used for separation. The following SRM transitions were used for quantification in the negative ion mode: 87 *m/z* to 43 *m/z* (pyruvate), 89 *m/z* to 43 *m/z* (lactate), 808 *m/z* to 408 *m/z* (acetyl-coenzyme A), 766 *m/z* to 408 *m/z* (coenzyme A), 117 *m/z* to 73 *m/z* (succinate), 145 *m/z* to 101 *m/z* (α-ketoglutarate), 169 *m/z* to 97 *m/z* (dihydroxyacetone phosphate), 115 *m/z* to 71 *m/z* (fumarate), 133 *m/z* to 71 *m/z* (malate), 229 *m/z* to 97 *m/z* (pentose phosphates), 124 *m/z* to 80 *m/z* (taurine), 259 *m/z* to 97 *m/z* (hexose phosphates), 259 *m/z* to 97 *m/z* (hexose phosphates) and 191 *m/z* to 111 *m/z* (citrate). Data interpretation was performed using TraceFinder (Thermo Fisher Scientific). Authentic metabolite standards were used for determining collision energies and retention times and for validating experimental retention times by standard addition.

Mice

All animal procedures associated with this work were conducted after approval by the institutional ethical committees.

The following mouse lines were used: C57BL/6J, SLC7A11-KO[55] and littermate wild-type, B6.BKS(D)-Leprdb/J (*db/db*) and PDGFRα-H2B-eGFP reporter mice[56]. For the GDF15-KO mice, the embryonic stem cells (as in ref. [57]) were obtained from EUCOMM and newly generated in our transgenic mouse core facility. Mice were housed in individually ventilated cages at the VIB Center for Inflammation Research, in a specific pathogen-free animal facility. Mice were housed under 14:10 (light:dark) light cycles, at 21 °C and 60% humidity. These conditions are checked and maintained by vivarium staff daily. All experiments on mice were conducted according to institutional, national and European animal regulations. Animal protocols were approved by the ethics committee of Ghent University (EC file no. 2020-049).

Skin wounding and erastin regimen

Full-thickness wounds were made as previously described[56,58]. In brief, wounds were made on shaved back skin by using 8-mm punch biopsy needles (Stiefel Instruments) under analgesia and general anaesthesia in 8-week-old female C57BL/6J, B6.BKS(D)-Leprdb/J (db/db), GDF15-KO, SLC7A11-KO and control littermates. For wound healing experiments, assuming standard deviations of 10–15%, an experimental group of $n = 10$ is needed to obtain statistical power of 90% (significance level 0.05) and detect a difference between means of 20%, using two-tailed paired *t*-testing. No animals were excluded from any experiment.

For topical applications, mice were intradermally injected with IKE at 20 mg kg^{-1} in 100 µl PBS (MedChemExpress, HY-114481) or recombinant human GDF15 (0.7 mg kg^{-1} in 100 µl PBS; R&D Systems, 9279-GD-050) or RSL3 (20 mg kg^{-1} in 100 µl PBS; Selleckchem, S8155) or the respective vehicle controls (DMSO or 4 mM HCl in 100 µl PBS) at the time of wounding and for two consecutive days. For the experiments indicated as erastin regimen or vehicle regimen, 5 million apoptotic Jurkat cells were administrated once on day 0 in 50 µl PBS on top of back skin immediately after full-thickness excision biopsy. When indicated, the compounds CP-91149 (50 mg kg^{-1}) and 3-BP (50 mg kg^{-1}) were administrated topically on the wounds on day 0 to day 2. For the mice injected intradermally with supernatants from efferocytic DCs, supernatants from DCs cultured with apoptotic Jurkat cells for 16 h were collected, centrifuged to eliminate debris and frozen or lyophilized for preservation.

Histology and immunohistochemistry

Skin biopsies were fixed using 4% paraformaldehyde overnight. Following dehydration steps, samples were embedded in paraffin and sectioned at 10 μm thickness. Dewaxed paraffin skin sections were stained with haematoxylin and eosin stains or subjected to heat-mediated antigen retrieval (citrate buffer; pH 6), followed by blocking the endogenous peroxidase activity by peroxidase blocking solution (Dako, S2023). Blocking and antibody incubations were performed in 5% goat serum in antibody diluent (Dako, S2022). Apoptotic cells were evaluated with cleaved caspase-3 antibody (1: 100; Cell Signaling Technology 9664). Slides were incubated with secondary antibody followed and peroxidase activity was detected with diaminobenzidine substrate kit (Cell Signaling, 8059P). Nuclei were counterstained with haematoxylin staining. Cleaved caspase-3$^+$ positive cells were manually counted by using Zen software by Zeiss. Quantification of cleaved caspase-3$^+$ cells was done by an independent researcher, who was blinded to the genotypes or treatment.

Immunofluorescence

For immunofluorescence analysis of frozen tissue, mouse back skin was embedded in OCT and tissue blocks were sectioned (10 μm) with a cryostat and mounted on SuperFrost Plus slides (ThermoFisher). After sectioning, tissue was fixed in 4% paraformaldehyde for 1h. After fixation, tissue was washed with PBS and was blocked in buffer containing 5% normal goat serum, 1% bovine serum albumin, 1% fish gelatin, 0.3% Triton X-100 in PBS, for 2 h at room temperature before incubation in primary antibodies (1:500 ITGα5, clone 5H10-27, AB_394779; BD Biosciences or Ki67, clone SolA15, AB_10854564; ThermoFisher, 1:200 biotin anti-CD11c antibody, BD Pharmingen 553800, 1:200 anti-SLC7A11 antibody, developed in-house[59]), at 4 °C overnight. Samples were washed three times with PBS prior to incubation with secondary antibodies for 2 h at room temperature.

Immunoblotting

BMDC were seeded in 6-well plates at a concentration of 500,000 cells per well. After 12 h of treatment with 5 μM erastin (S7242, Bio-Connect) or DMSO control, cells were collected and lysed directly in sample buffer. After protein denaturation, SDS–PAGE was performed using 10% gradient Bis–Tris gels. Primary antibodies were used for overnight incubation, followed by 1 h incubation with secondary antibody and chemiluminescence detection. Antibodies were used at the following dilutions: 1:1,000 (anti-phospho-glycogen synthase (Ser641/Ser645) 07-817; Sigma, anti-GYS1 monoclonal antibody (J.18.5), MA5-15022; ThermoFisher, anti-PYGL polyclonal antibody 15851-1-AP; Proteintech, anti-AGL/α-glucosidase antibody (EPR8880), ab133720; Abcam); 1:5,000 (anti-β-actin antibody–loading control HRP; mAbcam 8226).

Statistical analysis

Statistical significance was determined using GraphPad Prism 9, using unpaired Student's two-tailed t-test, one-way ANOVA or two-way ANOVA. $^{*}P < 0.05$, $^{**}P < 0.01$, $^{***}P < 0.001$, $^{****}P < 0.0001$.

Reporting summary

Further information on research design is available in the Nature Research Reporting Summary linked to this paper.

Data availability

All of the sequencing data associated with this work have been deposited in public data bases. Any other related information is available upon request. Source data are provided with this paper.

51. Deckers, J. et al. Co-activation of glucocorticoid receptor and peroxisome proliferator-activated receptor-γ in murine skin prevents worsening of atopic march. *J. Invest. Dermatol.* **138**, 1360–1370 (2018).
52. Sepulveda, F. E. et al. Critical role for asparagine endopeptidase in endocytic Toll-like receptor signaling in dendritic cells. *Immunity* **31**, 737–748 (2009).
53. Wiernicki, B. et al. Excessive phospholipid peroxidation distinguishes ferroptosis from other cell death modes including pyroptosis. *Cell Death Dis.* **11**, 922 (2020).
54. Hoste, E. et al. OTULIN maintains skin homeostasis by controlling keratinocyte death and stem cell identity. *Nat. Commun.* **12**, 5913 (2021).
55. Sato, H. et al. Redox imbalance in cystine/glutamate transporter-deficient mice. *J. Biol. Chem.* **280**, 37423–37429 (2005).
56. Van Hove, L. et al. Fibrotic enzymes modulate wound-induced skin tumorigenesis. *EMBO Rep.* **22**, e51573 (2021).
57. Lambrecht, S. et al. Growth differentiation factor 15, a marker of lung involvement in systemic sclerosis, is involved in fibrosis development but is not indispensable for fibrosis development. *Arthritis Rheumatol.* **66**, 418–427 (2014).
58. Hoste, E. et al. Innate sensing of microbial products promotes wound-induced skin cancer. *Nat. Commun.* **6**, 5932 (2015).
59. Van Liefferinge, J. et al. Comparative analysis of antibodies to xCT (Slc7a11): forewarned is forearmed. *J. Comp. Neurol.* **524**, 1015–1032 (2016).

Acknowledgements We thank members of the Ravichandran laboratory and B. Wiernicki for discussions and input; T. L. Aaes for Triwise analysis, and the VIB-Transgenic Core, VIB-Flow Cytometry Core, VIB-Bioimaging Core and VIB-Nucleomics Core; and the VBCF Metabolomics Facility, Vienna, for metabolomics analysis. K.S.R. is supported by FWO (Odysseus grant G0F5716N, EOS DECODE 30837538), Special Research Fund UGent (iBOF BOF20/IBF/037), European Research Council (ERC) (grant agreement no. 835243), grants from NHLBI (P01HL120840), NIAID (R01AI159551), NIGMS (R35GM122542), and the Center for Cell Clearance/University of Virginia School of Medicine. G.v.L. is supported by Foundation against Cancer (STK 2014-142 and STK 2018-093) and FWO (G020216N). S.M. is supported by postdoctoral Marie Skłodowska-Curie Actions individual fellowship (800446) from the European Commission, Horizon 2020 Research and Innovation Framework Program, and E.H. is supported by an FWO postdoctoral fellowship and FWO research grant. Additional support was received through the FWO Postdoctoral Fellowship (1227220N to P.M.). Mouse images in Figs. 1a,g, 2b,g, 3a, 4g,j and Extended Data Fig. 7d (mitochondria and pyruvate transporter) created with BioRender.com. We thank Dr. Sato (Niigata University, Japan) for the Slc7a11 knockout mice.

Author contributions S.M. and K.S.R. designed all experiments and wrote the manuscript. S.M. performed most experiments. E.H. provided conceptual advice and help for skin wound healing experiments. P.M. helped design and assisted with the metabolism-related experiments, B.N.K. assisted with histology studies, and H.K.L.D.C. assisted with immunoblotting experiments. J.P. assisted with bioinformatic analysis. K.L., R.V.d.C., P.J., G.v.L., D.E. and A.M. provided mice, technical advice and input on the manuscript.

Competing interests The authors declare no competing interests.

Additional information

Supplementary information The online version contains supplementary material available at https://doi.org/10.1038/s41586-022-04754-6.

Correspondence and requests for materials should be addressed to Sophia Maschalidi or Kodi S. Ravichandran.

Peer review information *Nature* thanks the anonymous reviewers for their contribution to the peer review of this work.

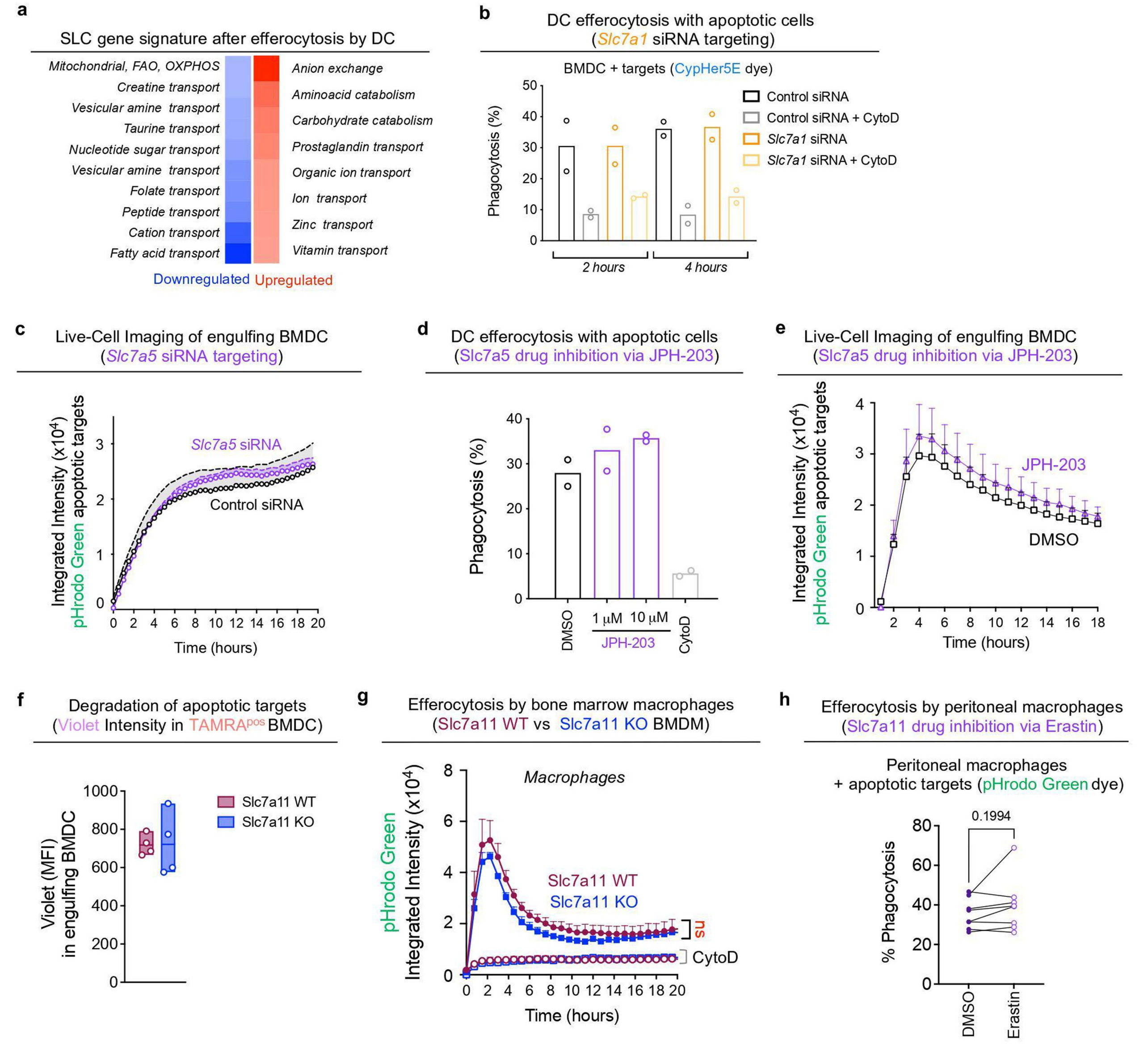

Extended Data Fig. 1 | Analyzing amino acid transporters during dendritic cell efferocytosis. **a**, SLC programs modulated in dendritic cells during efferocytosis of apoptotic cells compared to sterile phagocytosis. RNAseq was performed on primary BMDCs after engulfment apoptotic human Jurkat cells or beads. The heatmap illustrates SLCs upregulated and downregulated during dendritic cell efferocytosis. **b**, Uptake of CypHer5E- labelled apoptotic Jurkat cells by dendritic cells (BMDC) silenced for *Slc7a1* expression ($n = 2$ per condition). **c**, *Slc7a5* siRNA targeting in dendritic cells does not significantly affect apoptotic cell uptake as assessed by Incucyte Live-cell imaging ($n = 4$ per group). **d**, Efferocytosis of TAMRA-labelled apoptotic Jurkat cells by dendritic cells treated with different concentrations of the Slc7a5 inhibitor, JPH-203 ($n = 2$ per condition). **e**, Kinetics of efferocytosis by BMDC treated with 3 µM JPH-203 ($n = 3$ per condition). **f**, Measurement of degradation of TAMRA (pH insensitive) and Cell Trace Violet (pH sensitive) co-labelled apoptotic targets after efferocytosis by Slc7a11 KO and WT dendritic cells ($n = 4$ per group). Dendritic cells were incubated with apoptotic targets at a 1:5 phagocyte:target ratio for four hours. Floating bars show minimum to maximum values with all independent replicates, line denotes mean. **g**, Kinetics of efferocytosis by Slc7a11 WT and Slc7a11 KO bone marrow-derived macrophages with or without erastin treatment ($n = 4$ per group). ns: not significant; via One-way ANOVA with Tukey's multiple comparisons test. **h**, Efferocytosis by peritoneal macrophages after Slc7a11 inhibition via erastin. ($n = 8$ per condition; $P = 0.19$, with paired, two-tailed t-test). **c, e, g**, All live-cell imaging data are expressed as mean ± SEM.

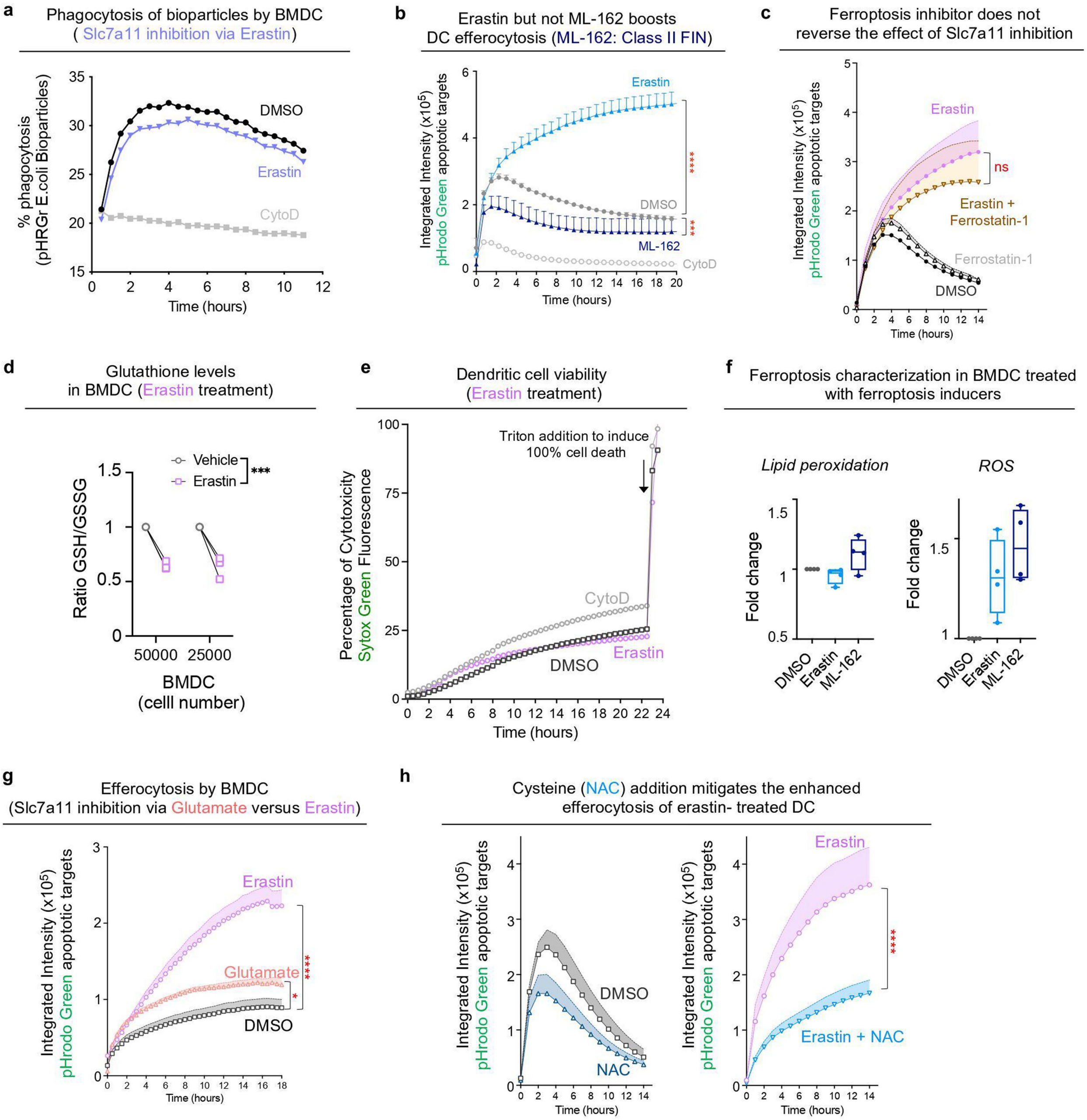

Extended Data Fig. 2 | Ferroptosis inducer and DC efferocytosis. **a**, Phagocytosis of E. *coli* bioparticles by dendritic cells measured at different time points with or without erastin treatment. Data are expressed as mean ± SD with $n = 2$ per condition. **b**, Ferroptosis inducer ML-162 does not enhance efferocytosis by dendritic cells. Live-cell imaging data are expressed as mean ± SEM ($n = 3$, DMSO and CytoD; $n = 4$, ML-162; $n = 6$, Erastin). **c**, Kinetics of efferocytosis by dendritic cells treated with antioxidant, Ferrostatin-1, erastin alone, or erastin + Ferrostatin-1 ($n = 4$ per condition, data are representative of two independent experiments). **d**, Measurement of glutathione levels in dendritic cells treated with erastin ($n = 3$ per condition, *** $P < 0.001$; via unpaired two-tailed *t*-test). **e**, Assessment of erastin drug cytotoxicity in dendritic cells by measuring Sytox Green fluorescence. Data are expressed as mean ± SD with $n = 2$ per condition. **f**, Measurement of lipid peroxidation and ROS (via C11-BODIPY and dihydrorhodamine 123 probes, respectively) in dendritic cells treated with ferroptosis inducers ($n = 3$ per condition). Results are expressed as fold change (FC). **g**, Direct comparison of kinetics of efferocytosis by dendritic cells treated with glutamate or erastin ($n = 4$, Glutamate and Erastin; $n = 8$, DMSO). **h**, Kinetics of efferocytosis after NAC, erastin alone or erastin + NAC treatment. DMSO was used as a vehicle control ($n = 7$, per condition). All live-cell imaging data (**b**, **c**, **g**, **h**) are expressed as mean ± SEM, * $P < 0.05$ *** $P < 0.001$; ****$P < 0.0001$; One-way ANOVA with Tukey's multiple comparisons test. ns: non-significant.

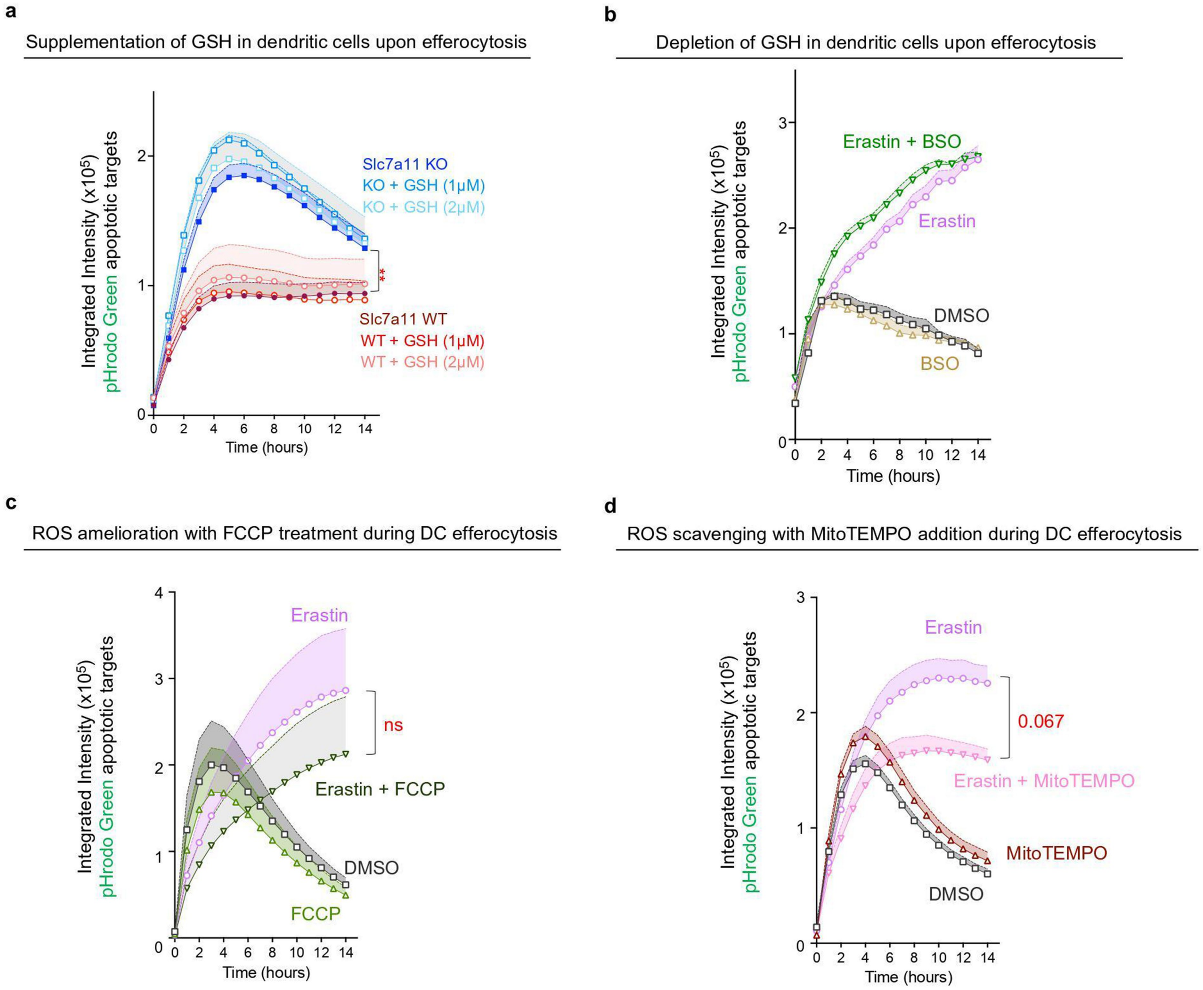

Extended Data Fig. 3 | Contribution of GSH and ROS in the context of enhanced efferocytosis by Slc7a11KO/inhibition. a, b, GSH supplementation or depletion does not affect the enhanced efferocytosis by DCs lacking Slc7a11 or treated with erastin. WT (*n* = 6) and Slc7a11 KO (*n* = 6) dendritic cells were supplemented with different concentrations of reduced GSH (*n* = 3 per concentration) (**a**), or treated with glutathione reducing compound, BSO (50 μM), erastin or erastin + BSO (**b**) (*n* = 3 per condition). DMSO was used as a vehicle control. Data are representative of 4 or 6 independent experiments, **c, d**, Interfering with ROS may be a component but is not sufficient to reverse the enhanced efferocytosis by Slc7a11 inhibited DCs. **c**, WT DCs were treated with 1 μM FCCP, together with erastin, erastin or DMSO alone (*n* = 7 per condition) or. **d**, WT DCs were treated with mitoTEMPO (100 μM; *n* = 4) for ameliorating and scavenging ROS respectively, together with erastin (*n* = 4) or erastin alone (*n* = 4). DMSO was used as a vehicle control (*n* = 3). Data are representative of three or five independent experiments. All live-cell imaging data are expressed as mean ± SEM (*P* = 0.067, ***P* < 0.01; ns: non-significant; One-way ANOVA with Tukey's multiple comparisons test).

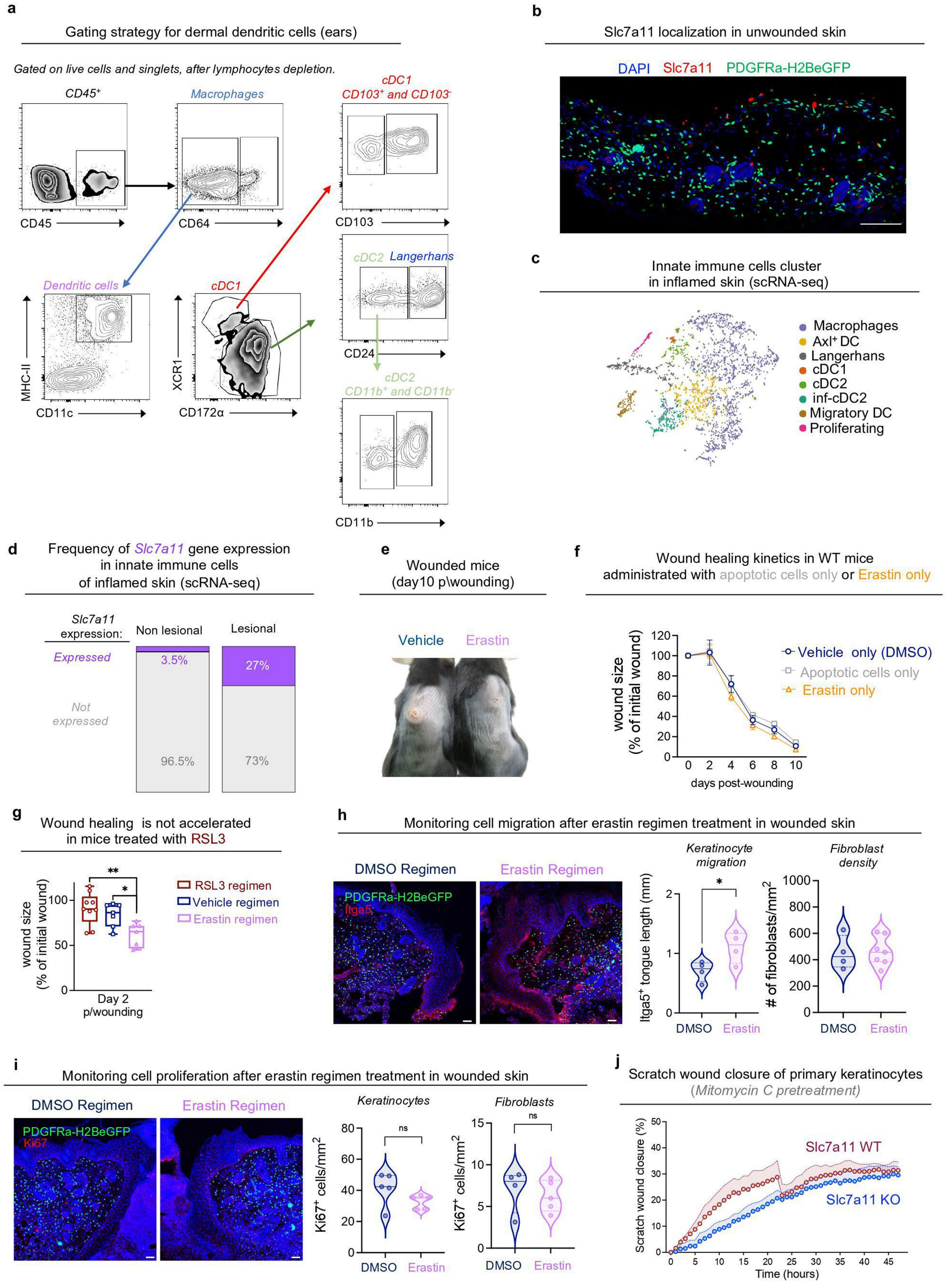

Extended Data Fig. 4 | See next page for caption.

Extended Data Fig. 4 | Analysis of dermal DCs and wound healing. **a**, Gating strategy of enriched phagocytes after digestion of ears and depletion of lymphocytes. **b**, Immunofluorescent images of skin sections from unwounded PDGFR-GFP mice depicting Slc7a11-positive (red) cells. Nuclei were stained with DAPI. Scale bar: 50 µm. **c**, Annotations of innate immune cell populations arising in lesional skin. **d**, Frequencies of *Slc7a11* expression in innate immune cells of lesional and non-lesional skin. **e**, Representative images of wounds of mice treated with erastin or vehicle at day 10 post-wounding. **f**, Wound healing dynamics comparing WT mice after full-thickness wounding and a single topical administration of apoptotic targets at the day of wounding or erastin and vehicle only at day 0 till day 2 ($n = 8$ per group). Data represent means ± SEM. **g**, Comparison of wound closure at day 2 post wounding in WT mice treated with RSL3 regimen ($n = 9$) versus erastin regimen ($n = 7$) or DMSO regimen ($n = 7$). Data represent means ± SEM.* $P < 0.05$; ** $P < 0.01$. One-way ANOVA with Tukey's multiple comparisons test. Box and whiskers show minimum to maximum values with all independent replicates, center denotes median. **h, i**, Erastin regimen promotes *in vivo* migration of keratinocytes during wound healing. PDGFRa-H2BeGFP mice were treated with erastin or DMSO regimen after full-thickness wounding with an 8 mm punch biopsy. Skin sections at day 4 post-wounding were stained with **h**, Itga5 ($n = 4$ per condition, keratinocytes; $n = 4$ DMSO-fibroblasts; $n = 7$ Erastin-fibroblasts) or **i**, Ki67 ($n = 4$ per condition, keratinocytes; $n = 4$ DMSO-fibroblasts; $n = 5$ Erastin-fibroblasts) Quantification (right) and representative immunofluorescent images (left) of skin sections with respective treatments. Nuclei were stained with DAPI (blue). Violins plots show minimum to maximum values with all independent replicates, centre denotes median. (*$P = 0.0420$; unpaired two-tailed t-test); ns:not-significant. Scale bar: 150 µm. **j**, Percentage of scratch wound closure (re-epithelialization) of mouse primary Slc7a11 WT ($n = 5$) and KO ($n = 4$) keratinocytes pretreated with mitomycin C. Slc7a11KO keratinocytes show no difference indicating that the effect on migration in vivo (**h**) is not cell intrinsic. Data are expressed as mean ± SD.

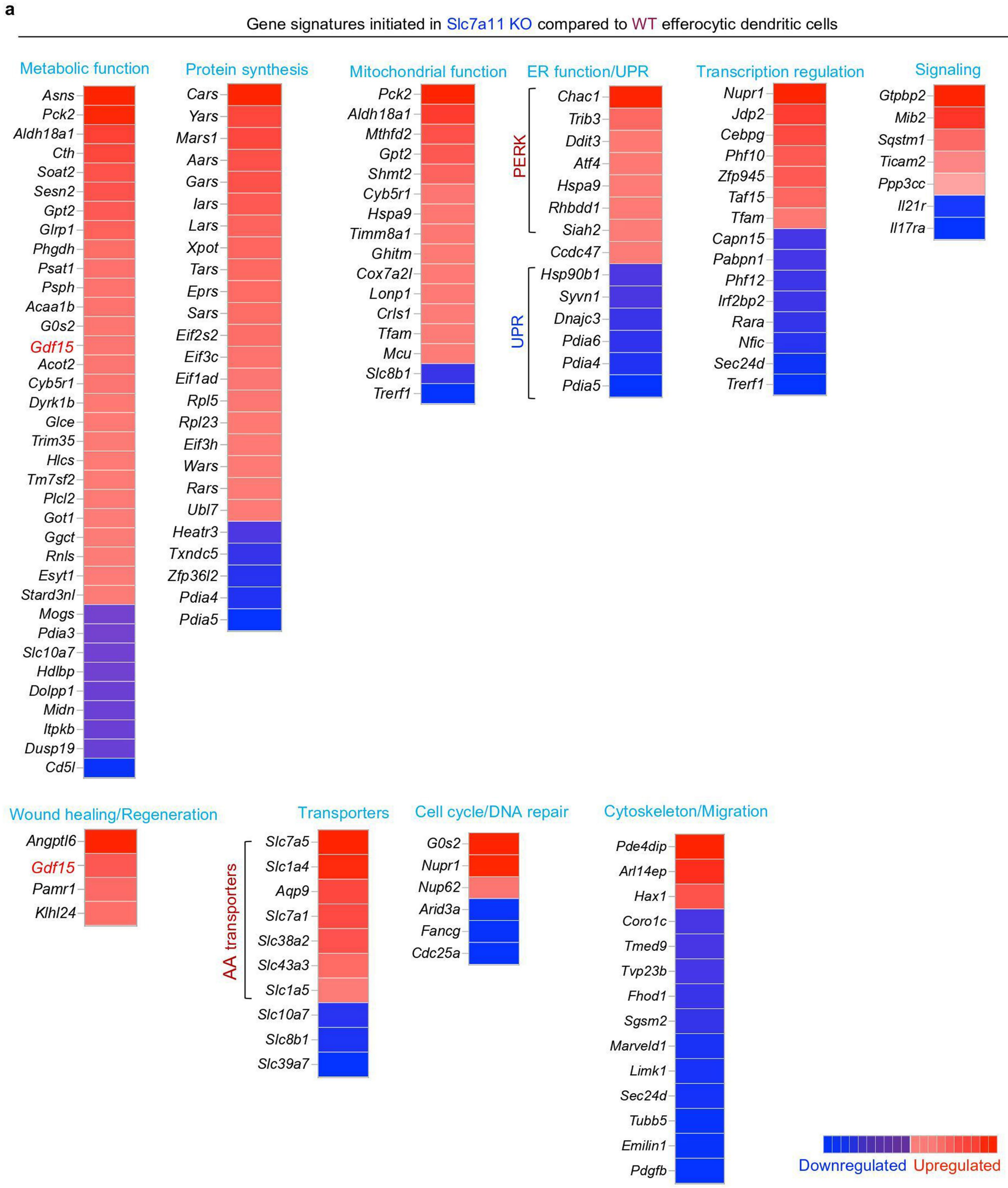

Extended Data Fig. 5 | Gene expression patterns in Slc7a11 KO efferocytic dendritic cells. a, Heat maps comparing efferocytic Slc7a11 KO versus WT dendritic cells showing upregulation and downregulation of differentially expressed genes (0.58 ≤ Log2FC ≤ −0.58) that are associated with metabolic and mitochondrial function, protein synthesis, ER homeostasis, transcription regulation, signaling, wound healing, cell cycle, migration and other transporters. Data are from 3-4 independent experimental replicates. *Gdf15* falls under the transcriptional programs of metabolic function and regeneration, and is highlighted in red.

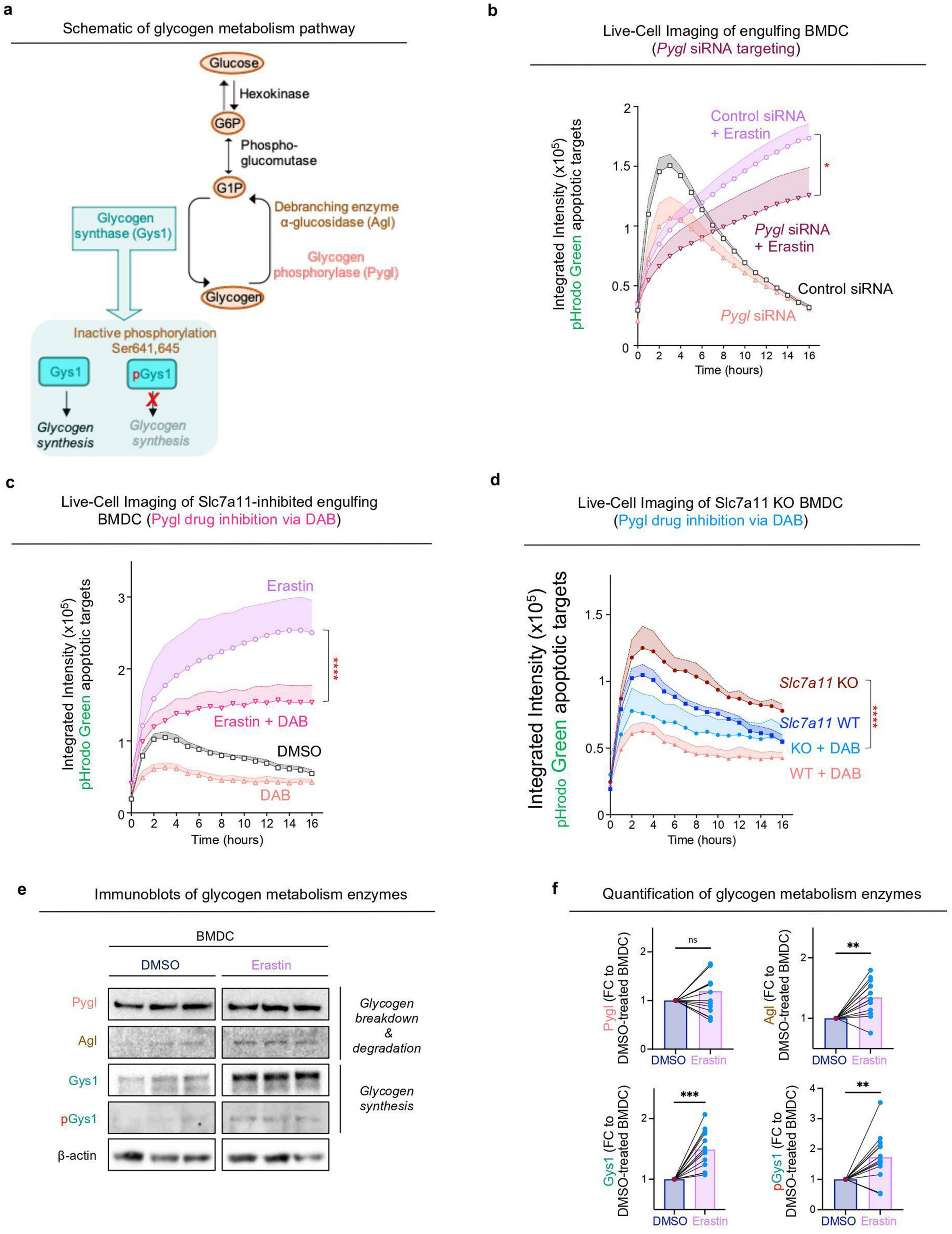

Extended Data Fig. 6 | See next page for caption.

Extended Data Fig. 6 | Glycogen pools are altered in the absence of Slc7a11 and affect DC efferocytosis. a, Schematic of glycogen metabolism pathway indicating the enzymes involved in glycogen breakdown, degradation and synthesis. In box, it is illustrated the inhibitory phosphorylation of Ser641, Ser645 and Ser649 on Gys1 which leads to decreased glycogen synthesis. **b**, *Pygl* siRNA targeting in dendritic cells compromises enhanced efferocytosis of Slc7a11-inhibited DCs. Live-cell imaging are expressed as mean ± SEM with $n = 4$ per condition, and are representative of two independent experiments. $^{*}P < 0.05$; One-way ANOVA with Tukey's multiple comparisons test. **c**, **d**, PYG inhibition via DAB compromises enhanced efferocytosis of Slc7a11-inhibited (**c**) or Slc7a11-KO DCs (**d**). Live-cell imaging are expressed as mean ± SEM with $n = 3$ per condition, and are representative of two independent experiments. $^{****}P < 0.0001$; One-way ANOVA with Tukey's multiple comparisons test. **e**, **f**, Representative immunoblot (**e**) and quantification of glycogen metabolism enzymes (**f**). Data are expressed as fold change (FC) of erastin-treated BMDC to DMSO control with $n = 14$;Pygl and $n = 13$;Agl, Gys1, pGys1; $^{**}P < 0.01$; $^{***}P < 0.001$, ns: non-significant via paired, two-tailed t-test.

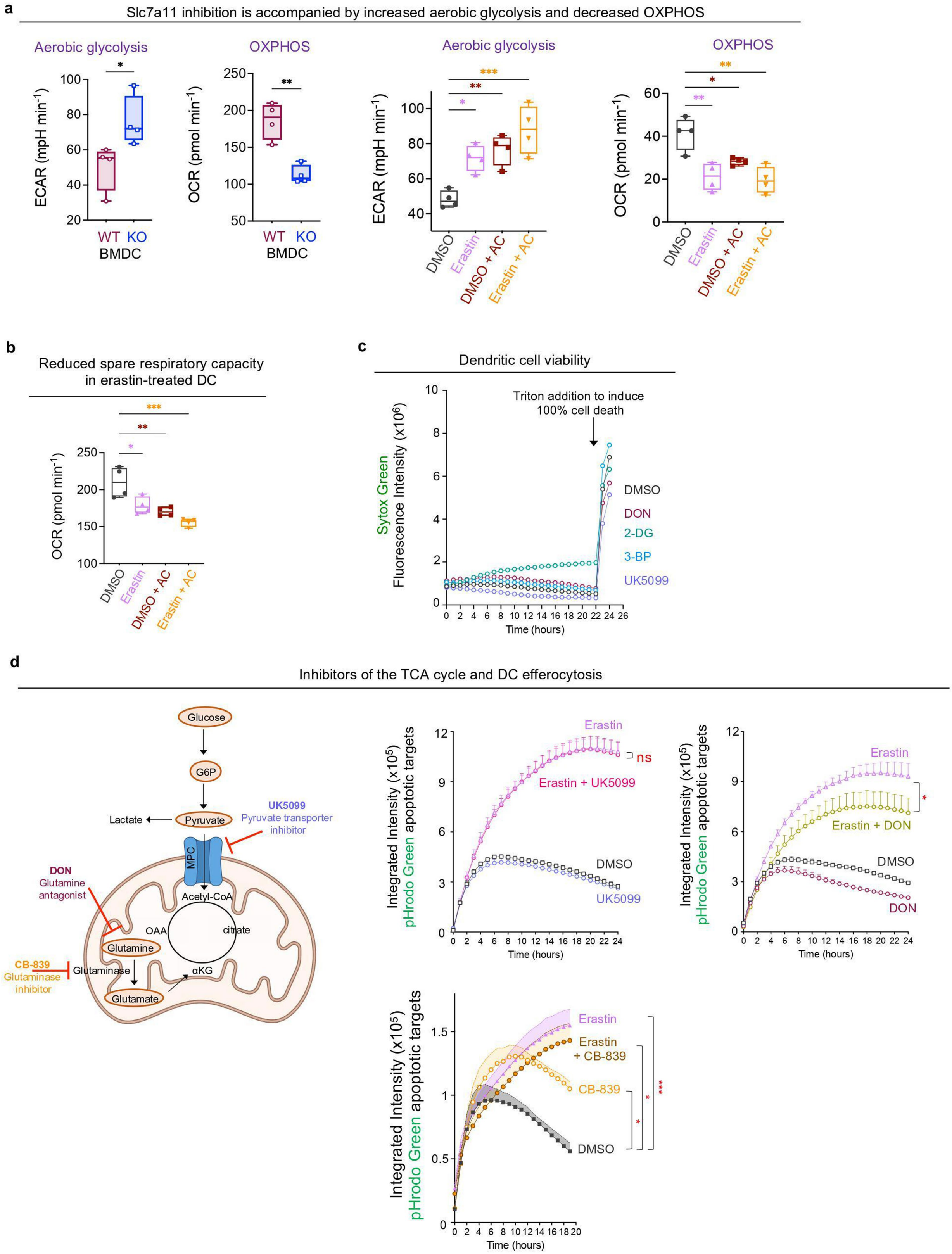

Extended Data Fig. 7 | See next page for caption.

Extended Data Fig. 7 | Metabolic inhibitors and DC efferocytosis. **a**, Increased aerobic glycolysis in dendritic cells during apoptotic cell clearance and Slc7a11 inhibition. Glycolysis and OXPHOS were measured at resting dendritic cells or during efferocytosis using Seahorse XF via extracellular acidification rate (ECAR) and oxygen consumption rate (OCR). Data represent means ± SEM of $n = 4$ per group; $^{*}P < 0.05$; $^{**}P < 0.01$; $^{***}P < 0.001$; $^{****}P < 0.0001$ via unpaired, two-tailed *t*-test or Two-way ANOVA with Tukey's multiple comparisons test. AC: Apoptotic Cells. **b**, Spare capacity was measured in dendritic cells after vehicle or erastin-treatment or during efferocytosis (with Seahorse XF) using oxygen consumption rate (OCR). Data from $n = 4$ per group; $^{*}P < 0.05$; $^{**}P < 0.01$; $^{***}P < 0.001$, via One-way ANOVA with Tukey's multiple comparisons test. AC: Apoptotic Cells. Box and whiskers (**a**, **b**) show minimum to maximum values with all independent replicates, center denotes median. **c**, Assessment of cytotoxicity of drugs tested on dendritic cells by measuring Sytox Green fluorescence $n = 4$; DMSO, 2-DG, 3-BP; $n = 2$; UK5099, DON. **d**, Kinetics of efferocytosis by WT BMDC treated with the indicated inhibitors DON ($n = 3$; DMSO, Erastin, DON, DON+ Erastin) or UK5099 ($n = 3$; DMSO, Erastin, UK5099, UK5099+ Erastin) or CB-839 ($n = 3$; DMSO, CB-839; $n = 6$; Erastin, CB-839+ Erastin) (see schematic representation) alone or in combination with erastin. DMSO was used as a vehicle control. All live-cell imaging data are expressed as mean ± SEM and are representative of four independent experiments ($^{*}P < 0.05$; $^{***}P < 0.001$; ns: not significant via One-way ANOVA with Tukey's multiple comparisons test).

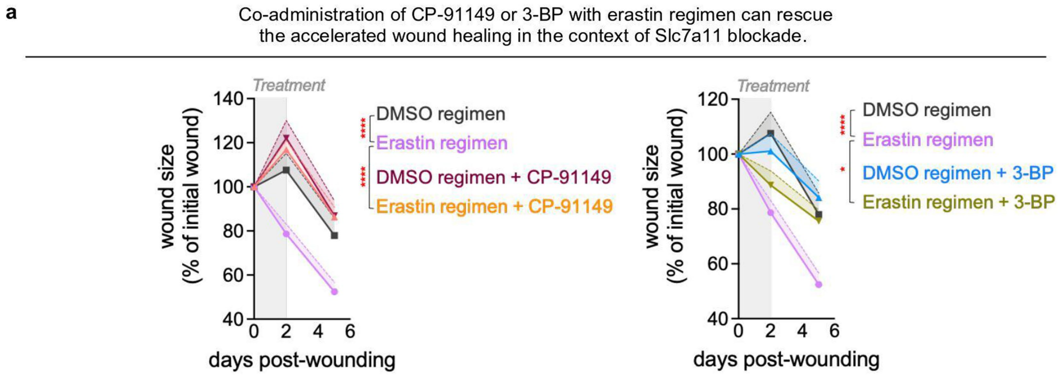

Extended Data Fig. 8 | Glycolysis/glycogen pathway inhibitors and wound healing. a, Co-administration of CP-91149 or 3-BP with erastin regimen can reverse the accelerated wound healing in the context of Slc7a11 blockade. Wound healing dynamics of wild-type mice treated with erastin regimen or vehicle regimen consisting of a single administration to the wound site of apoptotic cells at day 0 along with erastin or DMSO vehicle given on day 0 to day 2. When indicated, the compounds CP-91149 and 3-BP were topically administered on the wounds, on day 0 to day 2. Data represent means ± SEM and show one out of two independent experiments with $n = 9$; DMSO regimen, $n = 10$; Erastin regimen, $n = 8$; DMSO regimen + CP-91149 or 3-BP, $n = 8$; Erastin regimen + CP-91149 or 3-BP (* $P < 0.05$; **** $P < 0.0001$ via Two-way ANOVA with Tukey's multiple comparisons test).

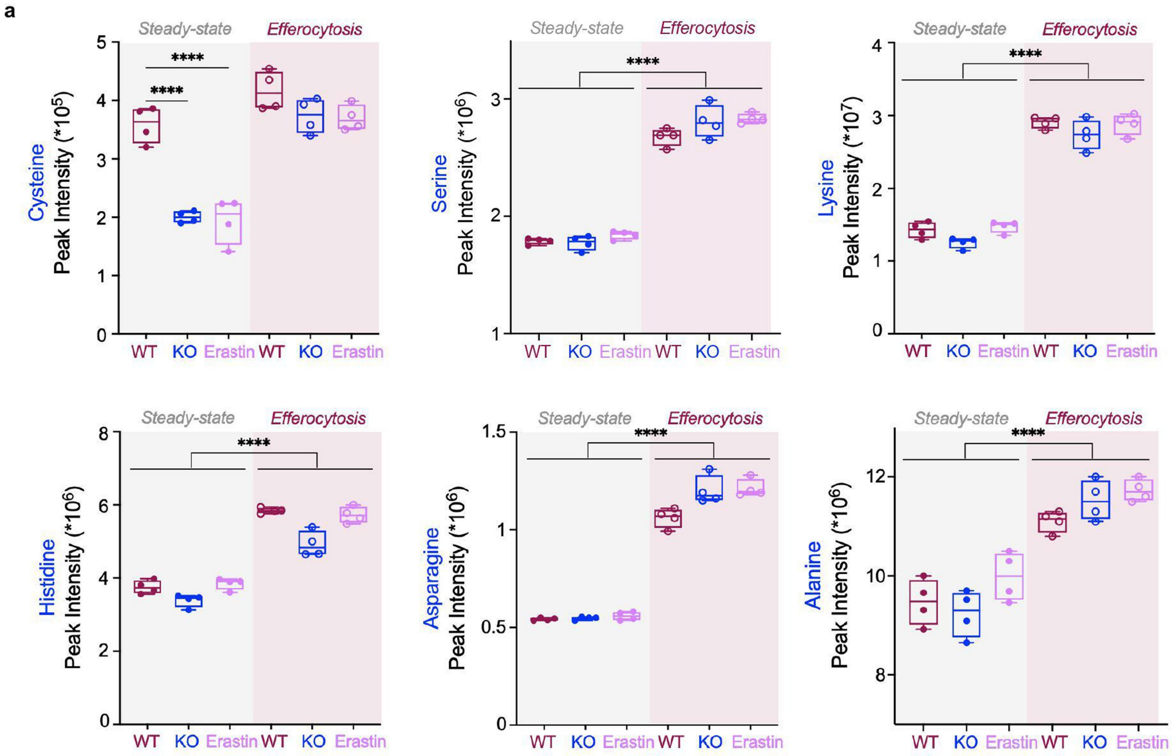

Extended Data Fig. 9 | Targeted metabolomics profiling in Slc7a11-null or inhibited DC. a, Peak intensity of several metabolites (absolute concentrations via targeted metabolomics) in the pellet of WT, Slc7a11 KO, and erastin-treated dendritic cells at steady state or upon efferocytosis (*n* = 4 biological replicates per condition; ****$P < 0.0001$ via One-way ANOVA with Tukey's multiple comparisons test). Box and whiskers show minimum to maximum values with all independent replicates, center denotes median.

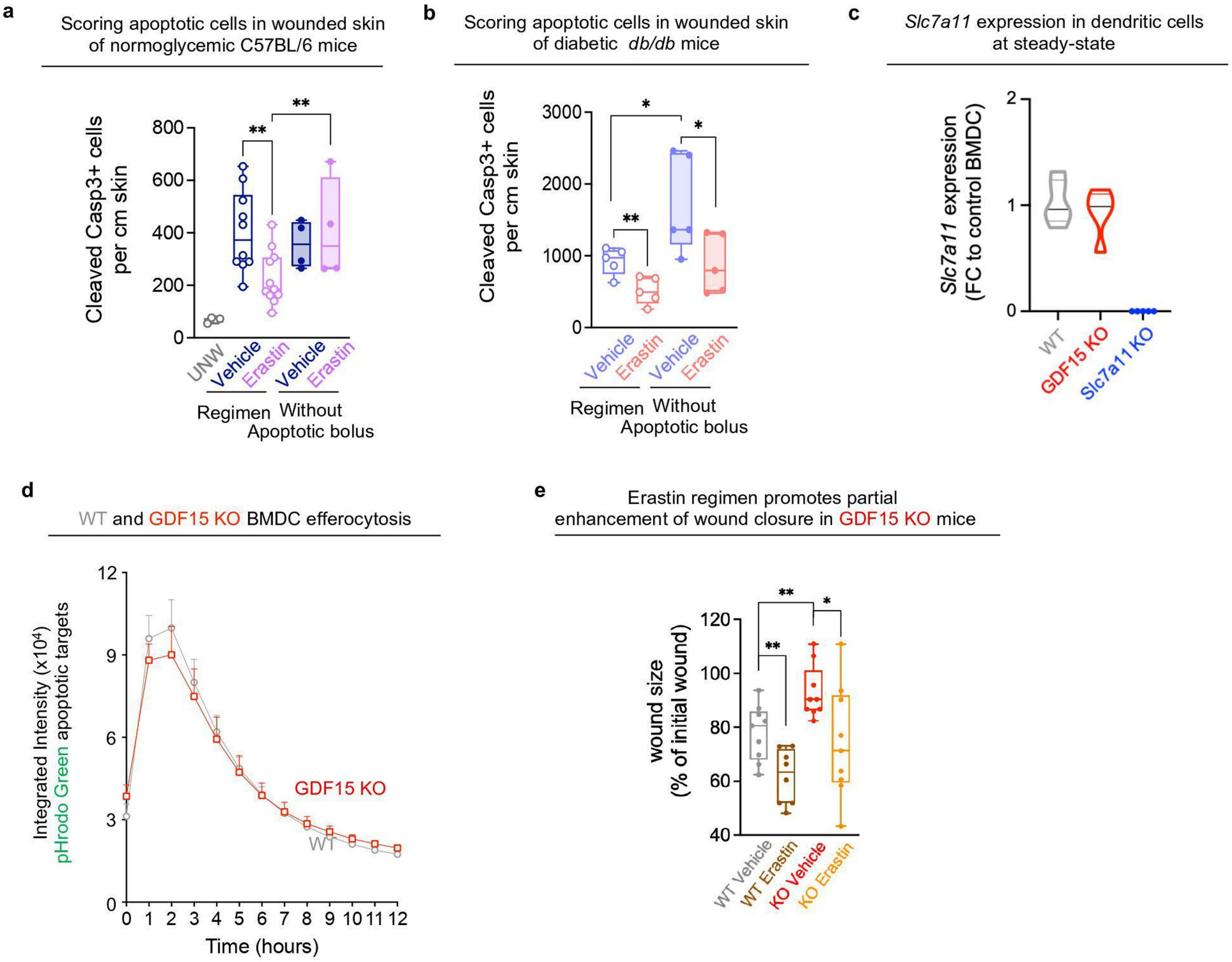

Extended Data Fig. 10 | Erastin ameliorates corpse clearance in the wounds of *db/db* mice and promotes partial wound healing in GDF15 KO mice. **a**, **b**, Erastin ameliorates corpse clearance with or without the addition of apoptotic bolus in in the wounds of *db/db* mice. Quantification of apoptotic cleaved caspase-3$^+$ cells in wounded skin of **a**, normoglycemic (B6) mice at day 4 post-wounding and **b**, diabetic (*db/db*) mice at day 8 post-wounding treated with erastin or vehicle regimen versus erastin or DMSO (for vehicle control) without the single administration of the apoptotic bolus. (B6: *n* = 4; UNW; *n* = 10; Vehicle regimen; *n* = 11; Erastin regimen; *n* = 4; Vehicle or Erastin; *db/db*: *n* = 5 mice per group; $^*P < 0.05$; $^{**}P < 0.01$ with unpaired, two-tailed *t*-test). **c**, Lysates were prepared using bone-marrow derived dendritic cells from WT, GDF15 KO and Slc7a11 KO mice, mRNA was isolated, followed by RT-qPCR analysis for *Slc7a11*. (*n* = 5 per genotype; data are presented as fold change to *Slc7a11* expression to control (WT) BMDC). **d**, GDF15 deficiency does not impair DC efferocytosis. Kinetics of efferocytosis by GDF15 KO and WT BMDC. Live-cell imaging data are expressed as mean ± SEM with *n* = 12; WT, *n* = 8; GDF15KO. **e**, Erastin regimen promotes partial wound healing in GDF15 KO mice. Wound healing dynamics comparing GDF15 KO and littermate control mice treated with erastin or DMSO vehicle given on day 0 to day 2. All wound sizes are expressed as percentage of initial wound size at day 2 post-wounding. (*n* = 8; WT+Erastin, *n* = 9; WT+vehicle, KO+Vehicle, KO+Erastin; $^*P < 0.05$; $^{**}P < 0.01$; between groups, via unpaired, two-tailed *t*-test. Violin plots (**c**), and the box and whiskers plots (**a**, **b**, **e**) show the minimum to maximum values with all independent replicates, center denotes median.

Extended Data Table 1 | Top 10 predictions for Slc7a11 associated diseases via ARCHS[4]

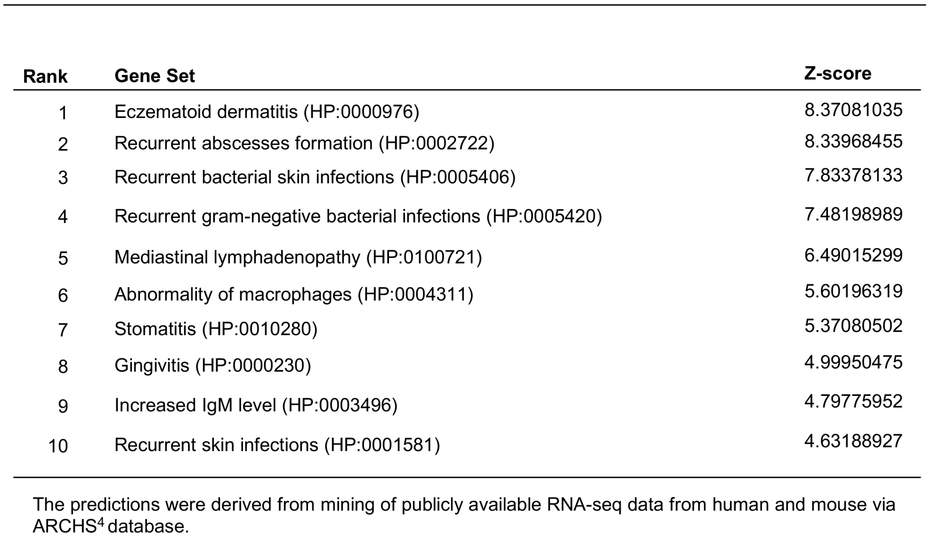

Rank	Gene Set	Z-score
1	Eczematoid dermatitis (HP:0000976)	8.37081035
2	Recurrent abscesses formation (HP:0002722)	8.33968455
3	Recurrent bacterial skin infections (HP:0005406)	7.83378133
4	Recurrent gram-negative bacterial infections (HP:0005420)	7.48198989
5	Mediastinal lymphadenopathy (HP:0100721)	6.49015299
6	Abnormality of macrophages (HP:0004311)	5.60196319
7	Stomatitis (HP:0010280)	5.37080502
8	Gingivitis (HP:0000230)	4.99950475
9	Increased IgM level (HP:0003496)	4.79775952
10	Recurrent skin infections (HP:0001581)	4.63188927

The predictions were derived from mining of publicly available RNA-seq data from human and mouse via ARCHS[4] database.

The predictions were derived from mining of publicly available RNA-seq data from human and mouse via ARCHS[4] database.

nature portfolio

Corresponding author(s): Kodi S. Ravichandran

Last updated by author(s): Mar 9, 2022

Reporting Summary

Nature Portfolio wishes to improve the reproducibility of the work that we publish. This form provides structure for consistency and transparency in reporting. For further information on Nature Portfolio policies, see our Editorial Policies and the Editorial Policy Checklist.

Statistics

For all statistical analyses, confirm that the following items are present in the figure legend, table legend, main text, or Methods section.

n/a	Confirmed	
☐	☒	The exact sample size (*n*) for each experimental group/condition, given as a discrete number and unit of measurement
☐	☒	A statement on whether measurements were taken from distinct samples or whether the same sample was measured repeatedly
☐	☒	The statistical test(s) used AND whether they are one- or two-sided *Only common tests should be described solely by name; describe more complex techniques in the Methods section.*
☒	☐	A description of all covariates tested
☐	☒	A description of any assumptions or corrections, such as tests of normality and adjustment for multiple comparisons
☐	☒	A full description of the statistical parameters including central tendency (e.g. means) or other basic estimates (e.g. regression coefficient) AND variation (e.g. standard deviation) or associated estimates of uncertainty (e.g. confidence intervals)
☐	☒	For null hypothesis testing, the test statistic (e.g. *F*, *t*, *r*) with confidence intervals, effect sizes, degrees of freedom and *P* value noted *Give P values as exact values whenever suitable.*
☒	☐	For Bayesian analysis, information on the choice of priors and Markov chain Monte Carlo settings
☒	☐	For hierarchical and complex designs, identification of the appropriate level for tests and full reporting of outcomes
☒	☐	Estimates of effect sizes (e.g. Cohen's *d*, Pearson's *r*), indicating how they were calculated

Our web collection on statistics for biologists contains articles on many of the points above.

Software and code

Policy information about availability of computer code

Data collection	Flow cytometry was performed using the BD LSR Fortessa cytometer. Cell sorting was performed using FACS ARIAII and III (BD Biosciences). Seahorse analysis was performed using Agilent Seahorse XFe96 analyzer. Live-cell imaging was performed using Incucyte ® ZOOM. RNA sequencing was performed using IlluminaNovoseq6000 platform by Novogene. Microscopy slides were imaged with an Axio Scan.Z1 (Zeiss, Jena, Germany), using a 10X Plan-Apochromat 0.45 NA (0.650 µm/pixel) and a Hamamatsu Orca Flash camera or by using Zeiss LSM880 fast AiryScan.
Data analysis	We used the following software packages for statistical and graphical analysis: GraphPad Prism version 9, FlowJo v.10, edgeR (Bioconductor), an add-on software module for the IncuCyte® Live-Cell Analysis System, DESeq2 software, RStudio Version 1.2.1335, Triwise package, Zen software by Zeiss. RNAseq analysis included: R package Rsubread and DESeq2 (Bioconductor). HISAT2 was selected to map the filtered sequenced reads to the reference genome. BAM files containing mapping results were counted using the feature Counts function in the R package Rsubread.

For manuscripts utilizing custom algorithms or software that are central to the research but not yet described in published literature, software must be made available to editors and reviewers. We strongly encourage code deposition in a community repository (e.g. GitHub). See the Nature Portfolio guidelines for submitting code & software for further information.

Data

Policy information about availability of data

All manuscripts must include a data availability statement. This statement should provide the following information, where applicable:

- Accession codes, unique identifiers, or web links for publicly available datasets
- A description of any restrictions on data availability
- For clinical datasets or third party data, please ensure that the statement adheres to our policy

Data Availability. Data presented in this study are availabile on ImmGen Microarray V1 data set "GSE15907" or publicly available RNA-seq data from human and mouse via ARCHS4 database (https://maayanlab.cloud/archs4/index.html). Single-cell RNA-sequencing datasets are are fully described in Hoste et al., (Hoste, E., Lecomte, K., Annusver, K., Vandamme, N., Roels, J., Maschalidi, S., Verboom, L., Vikkula, H. K., Sze, M., Van Hove, L., Verstaen, K., Martens, A., Hochepied, T., Saeys, Y., Ravichandran, K., Kasper, M. & van Loo, G. OTULIN maintains skin homeostasis by controlling keratinocyte death and stem cell identity. Nat Commun 12, 5913, doi: 10.1038/s41467-021-25944-2 (2021). For RNA-sequencing, the paired reads were aligned to reference genome of Mus musculus (GRCm38-mm10).

Field-specific reporting

Please select the one below that is the best fit for your research. If you are not sure, read the appropriate sections before making your selection.

☒ Life sciences ☐ Behavioural & social sciences ☐ Ecological, evolutionary & environmental sciences

For a reference copy of the document with all sections, see nature.com/documents/nr-reporting-summary-flat.pdf

Life sciences study design

All studies must disclose on these points even when the disclosure is negative.

Sample size	No statistical tests were used to determine sample size. For in vitro, ex vivo, and in vivo experiments, sample sizes were determined based on the numbers required to achieve statistical significance using indicated statistics, but with a minimum of 3 independently performed experiments to ensure data reproducibility. an experimental sample size of 10 mice per condition is needed and sufficient to result in scientifically relevant results. For wound healing experiments, assuming standard deviations of 10– 15%, an experimental group of n = 10 is needed to obtain statistical power of 90% (significance level 0.05) and detect a difference between means of 20%, using two-tailed paired T-testing.
Data exclusions	No data or no animals were excluded from any experiment.
Replication	Consistent results obtained from more than two technical replicates per experiment. Each experiments used at least 3-4 biological replicates. In vivo experiments were obtained from the given number of animals from at least 2 distinct cohorts/litters.
Randomization	Allocation of mice was random in all in vivo experiments, taken from littermates. Studies were performed in different vivaria (VIB-UGent Center for Inflammation Research, and UGent facility). All in vitro, experimental treatment group allocation was random.
Blinding	The investigators were not blinded to allocation during the experiments and outcome assessment. All experiments required known injections of substances, including drugs. Therefore, it was not possible to blind the investigator for such experiments. Hilstology quantification was done by an independent researcher, who was blinded to the genotypes or treatment.

Reporting for specific materials, systems and methods

We require information from authors about some types of materials, experimental systems and methods used in many studies. Here, indicate whether each material, system or method listed is relevant to your study. If you are not sure if a list item applies to your research, read the appropriate section before selecting a response.

Materials & experimental systems

n/a	Involved in the study	
☐	☒	Antibodies
☐	☒	Eukaryotic cell lines
☒	☐	Palaeontology and archaeology
☐	☒	Animals and other organisms
☒	☐	Human research participants
☒	☐	Clinical data
☒	☐	Dual use research of concern

Methods

n/a	Involved in the study	
☒	☐	ChIP-seq
☐	☒	Flow cytometry
☒	☐	MRI-based neuroimaging

Antibodies

Antibodies used	CD24-AF488 or -eFluor450 (M1/69; #101816 or #48-0242-82), CD11b-BV605 (M1/70; #563015), CD26-FITC or -BV650 (H194-112; #559652 or #740474) , CD11c-BV711 (HL3; #563048), F4/80-BV785 (BM8; #123141), CD45-AF700 (30-F11; # 56-0451-82), MHCII (I-A/I-E)-eFluor780 (M5/114.15.2; #47-5321-82), CD172a (SIRP alpha)- PerCP-eFluor710 (P84; #46-1721-82), CD103-BUV395 (M290; #740238), CD64-BV421 or - PE/Cy7 (X54-5/7.1; #139309 or #139314), XCR1-BV650 (ZET; #148220), Fc receptor-blocking antibody CD16/CD32 (clone 2.4G2, #553142), cleaved caspase-3 antibody (Cell Signaling Technology #9664), biotin anti-CD11c Ab (BD Pharmingen #553800), anti-Slc7a11 Ab (in-house developed), streptavidin 594 AlexaFluor (TheroFischer)and donkey-anti-rabbit DyLight 488 (Abcam ab#96919), Anti-phospho-GlycogenSynthase (Ser641/Ser645) #07-817; Sigma, anti-GYS1 Monoclonal Antibody (J.18.5), #MA5-15022; ThermoFisher, anti-PYGL Polyclonal antibody #15851-1-AP; Proteintech, anti-AGL/Alpha-glucosidase antibody [EPR8880], #ab133720; Abcam, Anti-beta Actin antibody - Loading Control HRP; mAbcam #8226, Itgα5 (clone 5H10-27, #AB_394779; BD Biosciences), Ki67 (clone SolA15, #AB_10854564; ThermoFisher).
Validation	All antibody lots are routinely tested by the manufacturers, and each product comes with a certificate of analysis from the indicated vendor stating that the product has met all quality control standards. Anti-Slc7a11 Ab has been previously validated (in-house developed; Van Liefferinge, J. et al. Comparative analysis of antibodies to xCT (Slc7a11): Forewarned is forearmed. J Comp Neurol 524, 1015-1032, doi:10.1002/cne.23889 (2016)). All Immunoblot antibodies produced a band (or bands) of the expected molecular weight(s) for the target protein. All flow cytometry and immunofluorescence antibodies were validated after titration and by integrating positive and negative controls.

Eukaryotic cell lines

Policy information about cell lines

Cell line source(s)	Human Jurkat Cell E6.1 wereobtained from ATCC.
Authentication	Morphological shape of cell lines was monitored via microscopic examination.
Mycoplasma contamination	All cell lines used in the laboratory are regularly tested for mycoplasma contamination and tested negative. Additionally, all medias and serum lots used are regularly tested and tested negative.
Commonly misidentified lines (See ICLAC register)	No commonly misidentified cell lines were used.

Animals and other organisms

Policy information about studies involving animals; ARRIVE guidelines recommended for reporting animal research

Laboratory animals	WT C57BL/6 mice were purchased from Janvier Labs and B6.BKS(D)-Leprdb/J (db/db) from Charles River. For the GDF15KO mice, the ES cells (Lambrecht, S. et al. Growth differentiation factor 15, a marker of lung involvement in systemic sclerosis, is involved in fibrosis development but is not indispensable for fibrosis development. Arthritis Rheumatol 66, 418-427, doi:10.1002/art.38241 (2014)) were obtained from EUCOMM and newly generated in our transgenic mouse core facility. The Slc7a11KO mice were provided from Pr. Ann Massie and generated as decribed in Sato, H. et al. Redox imbalance in cystine/glutamate transporter-deficient mice. J Biol Chem 280, 37423-37429, doi:10.1074/jbc.M506439200 (2005). The PDGFRα-H2B-eGFP reporter mice were a kind gift from Pr. Esther Hoste (Van Hove, L. et al. Fibrotic enzymes modulate wound-induced skin tumorigenesis. EMBO Rep 22, e51573, doi:10.15252/embr.202051573 (2021). All mice used in this study were 8-12 week old. For wounding experiments, female 8-12 week old were used Littermates were used for all experiments involving knockout animals. Numbers of mice are provided within each figure legend in addition to the number of independent cohorts/litters used. Mice were housed under 14:10 (light:dark) light cycles, at 21 degrees (C), and 60% humidity. These conditions are checked and maintained by vivarium staff daily.
Wild animals	No wild animals.
Field-collected samples	No field collected samples.
Ethics oversight	All animal work was approved by the VIB-UGent Center for Inflammation Research Ethical Committee, and the University of Ghent Animal Ethics Committee (EC file #2020-049).

Note that full information on the approval of the study protocol must also be provided in the manuscript.

Flow Cytometry

Plots

Confirm that:

☒ The axis labels state the marker and fluorochrome used (e.g. CD4-FITC).

☒ The axis scales are clearly visible. Include numbers along axes only for bottom left plot of group (a 'group' is an analysis of identical markers).

☒ All plots are contour plots with outliers or pseudocolor plots.

☒ A numerical value for number of cells or percentage (with statistics) is provided.

Methodology

Sample preparation	Samples were filtered prior to staining and kept on ice during staining. All fluorescent antibodies were aliquoted in a sterile hood with minimal light exposure. Staining of samples were protected from light throughout.
Instrument	Flow cytometry was performed using the BD LSR Fortessa cytometer. Cell sorting was performed using FACS ARIAII and III (BD Biosciences).
Software	Data were analyzed using FlowJo v.10
Cell population abundance	Purity of isolated samples was obtained by antibody stain and FACS. Sample purity was greater than 90%.
Gating strategy	Gating for immune cell populations was done following viable cells discrimination using Fixable Viability Dye and doublet exclusion using FSCHxW and SSC-HxW. Representative flow plots are included in extended data.

☒ Tick this box to confirm that a figure exemplifying the gating strategy is provided in the Supplementary Information.